Mass-Transfer Models for Rapid Pressure Swing Adsorption Simulation

Richard S. Todd and Paul A. Webley
Dept. of Chemical Engineering, Monash University, Clayton, 3800, Victoria, Australia

DOI 10.1002/aic.10948
Published online July 17, 2006 in Wiley InterScience (www.interscience.wiley.com).

In this study, trends from an adsorption process simulator are compared against experimental results obtained from a Rapid Pressure Swing Adsorption (RPSA) pilot plant for the separation of air over a packed bed of LiLSX pellets. The primary purpose of this study was to examine the impact of two model formulations for intrapellet mass transfer on predicted process performance, the linear driving force model and a rigorous pellet model (the viscous flow plus dusty gas model intrapellet flux equation). Non-isothermal and non-isobaric behavior is maintained within the model formulation. Nine PSA data sets at cyclic steady state were measured, with total cycle time varying from 8 to 50 s. At the short cycle time, large discrepancies between the simple lumped model and the rigorous pellet model arose, with the rigorous pellet model tracking qualitative trends in pilot plant data more faithfully than the simple model. The accepted value for the dimensionless cycle time θ_i below which linear driving force models fail is 0.1. However, our data and models suggest that a more appropriate value would be 1.0. Below $\theta_i = 1.0$ the simple linear driving force model started to deviate from experimental data and the rigorous pellet model. This suggests that conclusions from studies of single pellets may not apply rigorously to packed beds of pellets in which each pellet is exposed to rapidly varying and coupled boundary conditions in which composition, pressure, and temperature all change with time. © 2006 American Institute of Chemical Engineers *AIChE J,* 52: 3126–3145, 2006
Keywords: linear driving force model, dusty gas model, transport in porous media, rapid pressure swing adsorption, simulation

Introduction

The last 20 years have seen rapid growth in the development of pressure swing adsorption, particularly in relation to three key process applications: air dehumidification, hydrogen enrichment, and air separation.[1-3] One particular technology, Rapid Pressure Swing Adsorption (RPSA), has shown recent advancements in process design and operation and is of interest because the process plant size decreases as cycling becomes more rapid.[4,5] There is great interest in simulating these processes to avoid the need to build and run a pilot plant for design and optimization work.

Correspondence concerning this article should be addressed to P. A. Webley at paul.webley@eng.monash.edu.au.

Mathematical models of varying complexity have been developed for predicting RPSA performance.[6-11] Very few studies, however, have investigated the predictive ability of a fully *D*iscretized *P*ellet *M*odel (DPM) using the dusty gas model flux equation incorporating viscous flow (we refer to this model here as VF+DGM) to describe process performance of an RPSA system. The reason for this reluctance is the extensive computational time required to converge the resulting set of differential equations describing mass and energy conservation for the packed bed to cyclic steady state. The impact of pressure drop on process performance as a function of cycle time for a non-isothermal, bulk adsorbing separation during an RPSA cycle has similarly received minimal attention across the published literature. It is the aim of this study to understand how the results from an adsorption simulator will deviate between the linear driving force and DPM approach to mass

transfer at cycle times approaching the RPSA limit. In addition, the isobaric vs. non-isobaric assumption on model predictions at the RPSA limit is compared. The system considered here is a 1-bed PSA containing a single layer of LiLSX molecular sieve zeolite (purchased from Zeochem) for the separation of a dehumidified stream of air, assumed to be a binary mixture of O_2 and N_2.

Intrapellet Mass Transport Models used for Adsorption Simulation

The conservation of mass for species i in an adsorption column operating under non-isothermal conditions takes on the following form, assuming cylindrical geometry:

$$\frac{1}{RT}\frac{\partial p_i^B}{\partial t} - \frac{p_i^B}{RT^2}\frac{\partial T}{\partial t} = -\frac{\partial}{\partial z}\left(\frac{p_i^B v_B}{RT}\right) + \frac{6}{d_P}\frac{(1-\varepsilon_B)}{\varepsilon_B} N_{i,d_P} \quad \text{for } i = 1 \ldots N_c \quad (1)$$

where R represents the ideal gas constant in J gmole^{-1} K^{-1}, T the temperature in K, p^B interpellet pressure in Pa, t time in s, z axial position in m, v_B interstitial gas velocity in m s^{-1}, ε_B interpellet void fraction, d_P the pellet diameter in m, N_{i,d_P} the flux of gas into and out of the pellets at the pellet surface in gmole m^{-2} s^{-1}, and N_c the number of components present in the system, which for this study is 2. For the rigorous mass transfer model, the pellets are discretized. The conservation equation within the pellets, described here using spherical geometry, takes on the following form:

$$\left(\frac{\varepsilon_P}{RT} + \rho_P \frac{\partial n_{i,eq}^P}{\partial p_i^P}\right)\frac{\partial p_i^P}{\partial t} + \sum_{j=1, j\neq i}^{N_c}\left(\rho_P \frac{\partial n_{i,eq}^P}{\partial p_j^P}\right)\frac{\partial p_j^P}{\partial t} + \left(\rho_P \frac{\partial n_{i,eq}^P}{\partial T} - \frac{\varepsilon_P p_i^P}{RT^2}\right)\frac{\partial T}{\partial t} = -\frac{1}{r^2}\frac{\partial}{\partial r}(r^2 N_i) \quad \text{for } i = 1 \ldots N_c \quad (2)$$

where ε_P defines the intrapellet void, $n_{i,eq}^P$ the amount adsorbed in gmole kg^{-1}, p^P intrapellet pressure in Pa, ρ_P pellet density in kg m^{-3}, r the radial coordinate within the pellet in m, and N the molar flux in gmole m^{-2} s^{-1}. A dual-site Langmuir isotherm is used here to describe $n_{i,eq}^P$. :

$$n_{i,eq}^P = \frac{m_{i,site\ 1} b_{i,site\ 1} \exp(Q_{i,site\ 1}/RT) p_i^P}{1 + \sum_{j=1}^{N_c}[b_{j,site\ 1}\exp(Q_{j,site\ 1}/RT)p_j^P]} + \frac{m_{i,site\ 2} b_{i,site\ 2} \exp(Q_{i,site\ 2}/RT) p_i^P}{1 + \sum_{j=1}^{N_c}[b_{j,site\ 2}\exp(Q_{j,site\ 2}/RT)p_j^P]} \quad (3)$$

$m_{i,site\ 1}$ and $m_{i,site\ 2}$ are the saturated adsorbed phase loading for sites 1 and 2, respectively, in gmole kg^{-1}; $b_{i,site\ 1}$ and $b_{i,site\ 2}$ are the pre-exponential factors for sites 1 and 2, respectively, in Pa^{-1}; and $Q_{i,site\ 1}$ and $Q_{i,site\ 2}$ are the heats of adsorption for sites 1 and 2, respectively, in J gmole^{-1}. The pellet model requires Eq. 2 to be discretized across the pellet domain using N_r spherical control volumes, with the VF+DGM describing gas transport between each control volume.

$$\frac{N_i}{D_{K,i}^e} + \sum_{j=1, j\neq i}^{N_c}\left(\frac{y_j^P N_i - y_i^P N_j}{D_{m,ij}^e}\right) = -\frac{1}{RT}\frac{\partial p_i^P}{\partial r} - \frac{p_i^P}{RT}\left(\frac{B^e}{\mu_P D_{K,i}^e}\right)\frac{\partial p^P}{\partial r} \quad \text{for } i = 1 \ldots N_c \quad (4)$$

D_K^e represents the effective Knudsen diffusion coefficient in m s^{-2}, y^P the intrapellet mole fraction, D_m^e the effective molecular diffusion coefficient in m s^{-2}, B^e the effective viscous flow coefficient in m^2, and μ_P the intrapellet viscosity in Pa s. The DPM, in conjunction with the VF+DGM, presents a set of N_c N_r ODEs that need to be solved at each cylindrical control volume within the adsorption bed.

The linear driving force model can be obtained from the rigorous model by appropriate averaging. Volume averaging Eq. 2 over the pellet radius reduces N_r to 1, requiring just N_c ODEs to be solved over each cylindrical control volume within the adsorption column:

$$\left(\frac{\varepsilon_P}{RT} + \rho_P \frac{\partial \tilde{n}_{i,eq}^P}{\partial \tilde{p}_i^P}\right)\frac{d\tilde{p}_i^P}{dt} + \sum_{j=1, j\neq i}^{N_c}\left(\rho_P \frac{\partial \tilde{n}_{i,eq}^P}{\partial \tilde{p}_j^P}\right)\frac{d\tilde{p}_j^P}{dt} + \left(\rho_P \frac{\partial \tilde{n}_{i,eq}^P}{\partial T} - \frac{\varepsilon_P \tilde{p}_i^P}{RT^2}\right)\frac{dT}{dt} = -\frac{6}{d_P} N_{i,d_P} \quad \text{for } i = 1 \ldots N_e \quad (5)$$

A tilde over a variable (~) indicates that parameter is volume averaged over the pellet. Applying Fick's first law of diffusion allows N_i (which is now evaluated at the surface of the pellet) to be decoupled within Eq. 4:

$$-\frac{6}{d_P} N_{i,d_P} = \frac{4 K_i D_i^e}{RT d_P^2}(p_i^B - \tilde{p}_i^P) \quad \text{for } i = 1 \ldots N_c \quad (6)$$

Coupling Eqs. 5 and 6 is termed here the partial pressure form of the linear driving force model (LDFP). The LDFP model rigorously accounts for the coupled nature of the equilibrium isotherm in addition to temperature deviations unlike the more traditional solid diffusion form of the LDF model. The introduction of K_i is equivalent to defining an intrapellet profile on $\tilde{p}_i^P$ to solve N_i at the pellet surface.[12] Do & Mayfield[12] indicate this intrapellet profile continually changes during a cycle so K_i can be effectively referred to as a "time-dependent LDF constant." While the LDFP model is somewhat simpler in application to the DPM, the LDFP model inherently contains some limiting assumptions at the RPSA limit.[13-15]

The conservation of energy is retained within the model formulation to account for temperature variations that occur due to the adsorption of a bulk component from the gas stream.[16] Non-isothermal effects become important when temperature variation from adsorption/desorption become significant enough to affect the resultant loading and, hence, performance. The temperature variation at a point in the bed is proportional to the product of the working capacity and the heat of adsorption. If both of these are "small," that is, adsorption of a trace component that is weakly adsorbed, then the temperature effects may be ignored. This is the case with modeling N2PSA, in which the oxygen is selectively adsorbed from air and is weakly adsorbed (a kinetic separation). Although oxy-

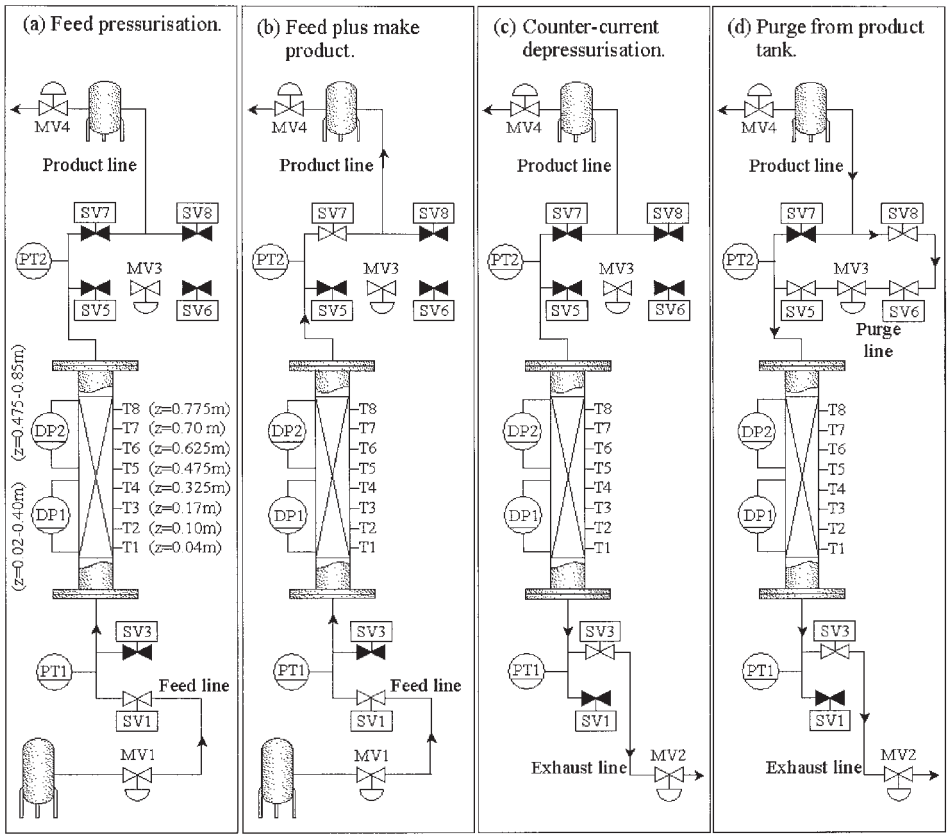

Figure 1. One-bed, four-step cycle initiated on the RPSA pilot plant.

(a) In step 1, gas from the feed tank is used to pressurize the sorbent bed. (b) When $p^{top} > p^{tank}$, step 2 starts and product gas is withdrawn from the column. (c) In step 3, the sorbent bed is depressurized to atmosphere. (d) In step 4, a small amount of gas from the product tank flows back through the bed as purge.

gen is not a trace component, it is relatively dilute (21% in air). On the other hand, in the present case, nitrogen is being adsorbed and is present as a bulk component (78%) with a reasonably large heat of adsorption (~30,000 J/gmole). The net result is that temperature profiles reveal variations in the bed by as much as 50 K. Given the sensitivity of the equilibrium adsorbed phase loading to temperature, a temperature variation of this magnitude cannot be neglected. The energy balance must, therefore, be included as:

$$\frac{\partial(\Sigma_{i=1}^{N_c}\rho_{g,i}^{B}U_{g,i}^{B})}{\partial t}+\frac{24(1-\varepsilon_B)}{\varepsilon_B}\int_0^{0.5d_P}\left[\varepsilon_P\frac{\partial(\Sigma_{i=1}^{N_c}\rho_{g,i}^{P}U_{g,i}^{P})}{\partial t}+\rho_P\frac{\partial(\Sigma_{i=1}^{N_c}U_{a,i}^{P})}{\partial t}+\rho_P\frac{\partial U_s^{P}}{\partial t}\right]\frac{r^2dr}{d_P^3}=-\frac{\partial}{\partial z}\left[\sum_{i=1}^{N_c}\left(\frac{p_i^{B}v_B}{RT}H_{g,i}^{B}\right)\right]-\frac{4h_{B,W}}{d_{bed}\varepsilon_B}(T-T_W) \quad (7)$$

$\rho_{g,i}^{B}$ and $\rho_{g,i}^{P}$ are the inter- and intrapellet gas phase density in gmole m^{-3}, $U_{g,i}^{B}$ and $U_{g,i}^{P}$ the inter- and intrapellet internal energy of the gas phase in J $gmole^{-1}$, $U_{a,i}^{P}$ and U_s^{P} the internal energy of the adsorbed and solid phases in J kg^{-1}, $H_{g,i}^{B}$ the enthalpy of the gas stream in J $gmole^{-1}$, $h_{B,W}$ the bed-to-wall heat transfer coefficient in W m^{-2} K^{-1}, d_{bed} the internal diameter of the adsorption column in m, and T_W the temperature of the adsorption column wall in K. Dynamic pressure profiles across a packed bed of adsorbent material can be modeled using the steady state Ergun equation.[17,18]

$$\frac{\partial p^{B}}{\partial z}=-\left[\frac{\kappa_{viscous}\mu_B}{d_P^2}\left(\frac{1-\varepsilon_B}{\varepsilon_B}\right)^2\right]v_B-\left[\frac{\kappa_{kinetic}\rho_g^{B}}{d_P}\left(\frac{1-\varepsilon_B}{\varepsilon_B}\right)\right]v_B|v_B| \quad (8)$$

Here $\kappa_{viscous}$ represents the numerical constant of the viscous term, $\kappa_{kinetic}$ the numerical constant of the kinetic term, and μ_B the interpellet viscosity in Pa s.

Experimental Apparatus and Cycle

All aspects of process design and operation of the experimental pilot plant introduced in this study can be found in Todd.[19] A schematic diagram of the system showing valving and the four-step cycle used in this study is shown in Figure 1. Product composition was measured using a Servomex 1440C paramagnetic oxygen analyzer. Calibration of this analyzer was performed using pure nitrogen, pure oxygen, and a 90 mol%O_2/10 mol%N_2 gas mixture. Plant operation is controlled

Table 1. Parameters That Were Controlled Around the RPSA Pilot Plant

Parameter of Interest	Target Value(s)	Valve Used to Achieve Target Value
Average product gas purity over cycle	80.0 ± 1.0 mol%O_2 90.0 ± 1.0 mol%O_2	Modulating valve on product line, MV4
Pressure at bottom of bed, end step 2[†]	400 ± 3 kPa	Modulating valve on feed line, MV1
Pressure at bottom of bed, end step 3[†]	120 ± 3 kPa	Modulating valve on exhaust line, MV2
Pressure at bottom of bed, end step 4[†]	140 ± 3 kPa	Modulating valve on purge line, MV3

Since two different pressure windows and product purities are considered, the first two entries in this table are set to one of two possible combinations.
[†]Note that the "bottom of bed" is represented by the void volume located between the packed bed interface and SV1 and SV3.

through a GE Fanuc 90–30 PLC that operates each valve while continually monitoring all analog input devices.

To minimize model mismatch that can potentially arise with asymmetrical profiles for two-bed operations,[20] a one-bed four-step cycle was used, as shown in Figure 1. Step 1 involves co-current pressurization from the bottom of the packed bed to the top with feed gas. Step 2, feed plus make product, begins when the pressure in the void space at the top of the sorbent bed is equal to or greater than product tank pressure. Although times for steps 1 and 2 were not pre-set before starting a run, the total time for these two combined steps was allocated half of the total cycle. This effectively means the time for which "adsorption" and "desorption" are being performed constitutes half of the total cycle time. At the completion of step 2, all solenoid valves on the top manifold are closed and the bed is depressurized in the counter-current direction from the top of the packed bed to the bottom through SV3 to atmosphere. Once the bed has reached a designated minimum in pressure, counter-current purge (step 4) is performed by allowing a small amount of product gas to flow back into the bed from the product tank while desorbed gas is still being withdrawn from the bottom of the column.

Target values for end of step pressures and product purity

When the RPSA pilot plant was running, one target purity and three target pressures were maintained at cyclic steady state (CSS) using each of the four modulating valves located around the plant (labeled MV1 through MV4 in Figure 1). A summary of these target values and the corresponding valve used to achieve that particular control target is provided in Table 1. Note the range for each target value on pressure is assigned as the uncertainty in each transducer reading. The lower pressure limit of 120 kPa was always maintained on step 3 to ensure the packed bed was higher than atmospheric pressure throughout the cycle; this avoids atmospheric air flowing back into the packed bed should the column completely depressurize before purge commences. Bed pressure increases slightly during purge so the pressure at the end of steps 2 and 3 defines the pressure window over which the cycle operates and, hence, two parameters to control. The high purity target of 90 mol%O_2 is a typical purity required from most industrial PSA plants.[21] This same target value also indicates a large majority of the MTZ should remain within the bed to maintain purity. Although the second purity target of 80 mol%O_2 is not so common industrially, this does allow partial breakthrough to occur and, hence, the MTZ is not necessarily confined to the packed bed.

End of step purge pressure, 140 kPa absolute, was an arbitrary value that was selected according to the following heuristics. An increase in pressure from the end of counter-current depressurization to purge was desired so that gas was always flowing in the negative z direction (that is, from the product tank to exhaust line) to ensure the nitrogen Mass Transfer Zone (MTZ) was pushed further back in the bed. The ensuing "feed plus make product" step will, therefore, commence with the upper region of the bed relatively clean when SV7 opens to the product tank. While pressure should increase, end of step purge pressure should not be too high with respect to the pressure window; otherwise, the bed will be over-purged. This means the volume of product gas passing back into the bed as purge is greater than the minimum required to maintain purity, with specific productivity and recovery decreasing as a result. From these two heuristics, end of step purge pressure is now a parameter that needs to be optimized for each cycle under consideration if process performance is the parameter of interest. Since we are not concerned with performance optimization in this study, we are not concerned with end of step purge pressure that corresponds to the optimal operating condition. Further to this, a reduction in cycle time may potentially alter optimum end of step purge pressure due to the changing influence of intrapellet mass transfer and interpellet pressure drop. For this reason, 140 kPa was deemed suitable without the need to perform additional runs at each cycle time and pressure window under investigation.

Cycle times investigated

The longest cycle time used on the RPSA pilot plant for which CSS could be maintained was 50 s. This time represents the slowest cycle performed in this study. As mentioned earlier, the combined times for steps 1 and 2 was half of t_{cycle}. The remaining two steps of the cycle used fixed step times. In assigning these times, it was arbitrarily stipulated that 12 to 14% of the cycle be devoted to purge to the nearest second. From this, the balance in cycle time was designated for step 3, counter-current depressurization. Table 2 provides a summary of the five cycle times investigated. Table 2 also provides an approximate estimate on the magnitude of the dimensionless time parameter θ_i commonly encountered in the RPSA literature. To calculate θ_i for nitrogen and oxygen, the Bosanquet assumption for combined intrapellet molecular and Knudsen diffusion was used.[22] Given this effective coefficient is often stated in surface diffusion form, a correction for the equilibrium isotherm derivative is required. The governing form of θ_i can be described analytically as follows:

Table 2. Individual Step and Cycle Times Considered on the RPSA Pilot Plant

Total Cycle Time (s)	Steps 1 and 2 Combined (s)	Step 3 (s)	Step 4 (s)	θ_i for Nitrogen (−)	θ_i for Oxygen (−)
50	25	19	6	≈4.2	≈11
36	18	13	5	≈3.0	≈8.5
22	11	8	3	≈1.9	≈5.2
14	7	5	2	≈1.2	≈3.3
8	4	3	1	≈0.7	≈1.9

Also included are the calculated values of θ_i for nitrogen and oxygen in each of these cycles.

$$\theta_i = \frac{4tD_i^e}{d_P^2} \equiv \frac{4t}{d_P^2}\left[\frac{\left(\dfrac{p^P\sigma_{ij}^2\Omega}{1.8829\times10^{-2}C_m\sqrt{T^3(M_i+M_j)/M_iM_j}} + \dfrac{1}{48.5C_K\delta}\sqrt{\dfrac{M_i}{T}}\right)^{-1}}{\varepsilon_P + \rho_P RT(\partial n_{i,eq}^P/\partial p_i^P)}\right] \quad \text{for } i = 1, 2 \text{ and } j \neq i \tag{9}$$

where D^e represents the average diffusion coefficient in m s^{-2}, σ the Lennard-Jones collision diameter in Angstrom, Ω the dimensionless collision integral, C_m the dimensionless structural parameter for molecular diffusion, M the molecular weight in g $gmole^{-1}$, C_K the dimensionless structural parameter for Knudsen diffusion, and δ the intrapellet pore diameter in m. Values of θ_i were obtained by assuming intrapellet gas is at "average" conditions: 300 kPa, 290 K, and feed composition (78 mol%N_2/22 mol%O_2). This number provides a first approach estimate to the definition of an RPSA cycle: Glueckauf,[23] Jury,[24] and Nakao and Suzuki[25] suggest $\theta_i < 0.1$ is RPSA. From these estimates, the shortest cycle time is close but still above this limit. With respect to industrial literature, the 22, 14, and 8 s cycle times are classified as RPSA cycles: Dangieri and Cassidy[26] and Wells[27] suggest $t_{cycle} < 30$ s is RPSA.

Simulating the RPSA Pilot Plant

Table 3 summarizes the physical dimensions of interest required to simulate the RPSA pilot plant, in addition to the physical properties of the adsorbent. For all simulations performed in this study, bottom and top void volume models were simulated as CSTR's and set to the corresponding experimental volume value shown in Table 3. V_{bottom} is the void volume between the bottom of the packed bed and the valve seats of SV1 and SV3. V_{top} is the void volume between the top of the packed bed and the valve seats of SV5 and SV7. In addition to this, p^{bottom} refers to the pressure in the void volume below the packed bed, p^{top} to the pressure in the void volume above the packed bed, and p^{tank} the pressure within the product tank. The adsorption columns are constructed from stainless steel 304 with a wall thickness of 0.0034 m. A rigorous energy balance over the metal walls of the adsorption column was included in the model formulation to account for the accumulation and conduction of energy along the walls. Leva's correlation was used to calculate a local heat transfer coefficient between the sorbent bed and wall at each axial coordinate inside the adsorption column.[28] External film heat transfer coefficients from the wall to ambient were set to zero since the adsorption column was wrapped with insulation.

Numerically, product flow per cycle is calculated from the accumulated moles obtained downstream of SV7 on step 2 minus the moles of gas passing back into the bed as purge on step 4. Hence, product gas purity is calculated as the ratio of oxygen to total flow obtained during step 2 of the cycle. After step 2 of each simulated cycle, the simulator updates product gas composition based on this ratio and passes this composition back into the top void on step 4.

With numerical valve coefficients controlled to achieve end of step pressure and purity targets, no fitting parameters remain to match experimental data. Equilibrium isotherm parameters,[19] intrapellet structural parameters,[29,30] and pressure drop coefficients[18] were determined independently. The isotherm for N_2 and O_2 on LiLSX was measured and correlated using the Dual-Site Langmuir Equation. Experimental profiles obtained

Table 3. A Summary of Experimental Parameters That Characterize the RPSA Pilot Plant and LiLSX Adsorbent Pellets Packed Within the Adsorption Column

Parameter	Magnitude	Units
m_{bed}	11.29 ± 0.5	kg
L_{bed}	1.00 ± 0.01	m
d_{bed}	0.156 ± 0.001	m
V_{bottom}	2.68 ± 0.05	$\times10^{-3}$ m^3
V_{top}	2.28 ± 0.05	$\times10^{-3}$ m^3
d_P	1.7 ± 0.2	$\times10^{-3}$ m
ρ_P	926 ± 77	kg m^{-3}
ε_P	0.62 ± 0.04	—
ε_B	0.35 ± 0.06	—
δ	2.5 ± 0.4	$\times10^{-7}$ m
C_K	0.083 ± 0.018	—
C_v	0.061 ± 0.026	—
C_m	0.166 ± 0.040	—
$\kappa_{viscous}$	154 ± 14	—
$\kappa_{kinetic}$	1.47 ± 0.13	—

Component	$m_{site\ 1}$ (gmole kg^{-1})	$b_{site\ 1}$ (kPa^{-1})	$Q_{site\ 1}$ (J $gmole^{-1}$)
Nitrogen	1.316 ± 0.020	(1.601 ± 0.015) × 10^{-6}	21,540 ± 50
Oxygen	1.316 ± 0.020	(2.727 ± 0.015) × 10^{-6}	13,550 ± 50
	$m_{site\ 2}$ (gmole kg^{-1})	$b_{site\ 2}$ (kPa^{-1})	$Q_{site\ 2}$ (J $gmole^{-1}$)
Nitrogen	1.625 ± 0.020	(4.379 ± 0.015) × 10^{-8}	26,410 ± 50
Oxygen	1.625 ± 0.020	(1.882 ± 0.015) × 10^{-6}	13,610 ± 50

Table 4. Magnitude of the Tolerances Applied to Each CSS Parameter When Simulating RPSA Pilot Plant Data

Parameter	Magnitude	Units
E_{max} for p_i^B	5.0	kPa for $i = 1 \ldots N_c$
E_{max} for n_i^P	2.0×10^{-4}	gmole kg^{-1} for $i = 1 \ldots N_c$
E_{max} for T	1.0×10^{-2}	K
E_{norm} for p_i^B	1.0	kPa for $i = 1 \ldots N_c$
E_{norm} for n_i^P	1.0×10^{-4}	gmole kg^{-1} for $i = 1 \ldots N_c$
E_{norm} for T	5.0×10^{-3}	K
E_1 and E_2	1.0×10^{-2}	%
E_{heat} and E_{diff}	1.0×10^{-1}	%

A complete definition of these parameters can be found in Todd et al.[31]

during pilot plant operation from the product tank have been used as boundary conditions in the simulator to fit product tank response. We are mainly concerned here with dynamics that reside within the adsorption column, not with detailed modeling of the pressure/temperature history of the product tank. Fitting this experimentally means errors in the product tank model do not manifest in any deviations observed numerically for the packed bed, allowing valid conclusions to be made regarding bed response that are independent of the tank model.

Our adsorption simulator employs a successive substitution approach to CSS from an arbitrary set of initial conditions over a predefined cycle arrangement. Initially, we use the simple linear driving force model to approach cyclic steady state; thereafter, the detailed mass transfer model is automatically activated in the simulator and the calculations progressed to cyclic steady state again. This avoids the need to compute all cycles with the detailed model. For all RPSA pilot plant simulations, the CSS check of Todd et al.[31] was used, with the magnitude of these parameters shown in Table 4.

Appropriate level of axial and radial discretization

One limitation inherent with numerical models and adsorption simulation is the appropriate level of axial discretization, N_z, required to suitably resolve all spatial profiles across the sorbent bed. In addition to this, Todd and Webley[30] revealed some dependence on the level of radial discretization within the pellet, N_r, for single step breakthrough experiments. A priori estimates on these parameters for the simulation of an RPSA cycle when producing oxygen enriched air are not generally available. From this point, an appropriate level of discretization across both domains had to be selected that:

(i) Allows a solution to be attained within a reasonable period of time (that is, does not require several months to attain a single CSS operating point), and

(ii) Adequately resolves spatial profiles to an accuracy that readily allows a number of comparisons to be made with experimental data at the interpellet level.

An axial discretization level of 41 nodes was found to be adequate to resolve spatial profiles across the interpellet domain of the sorbent bed ($N_z = 41$), while the radial domain of the pellet was discretized into five equal volumes ($N_r = 5$). Todd and Webley[30] show for $N_r = 5$, C_m should be set to 0.166, while C_K and C_v are 0.083 and 0.061, respectively. Resolving the axial domain into 41 volumes produces a node spacing of approximately 0.025 m. Spatial resolution does not need to be as fine for a cyclic process in relation to a breakthrough experiment given initial profiles are "smeared" as a result of the preceding counter-current depressurization and purge steps.[32] The finite volume method was used for spatial discretization of the axial bed and radial pellet domains. Webley and He[32] provide details on the numerical implementation of this scheme for adsorption simulation.

Implementing numerical control loops

Table 1 introduced four target values that are maintained during each run on the RPSA pilot plant. These same constraints were also imposed numerically in the form of proportional-only control loops.[33] The implementation of PID control loops within our simulator is discussed in Todd et al.[31] To ensure CSS data that are written to file also satisfy control targets values, the CSS check invoked numerically stipulates each control loop must be within tolerance, in addition to profile and mass/energy balance closure checks performed using parameters from Table 4. In general, an additional 500 to 1000 cycles were simulated once control loops had converged to achieve final CSS conditions. This means anywhere from 2,000 to 12,000 cycles were simulated in total per RPSA run.

Results: Comparison of RPSA Pilot Plant and Simulations

A select number of variables are used to distinguish one experimental pilot plant run from another. The most important of these, which are required when simulating each run, include:

(i) Product purity, reported in mol%O_2. This value was measured directly as one steady reading from the paramagnetic oxygen analyzer located on the product line at CSS. As binary component simulations are performed, product purity is also reported as mol%O_2+Ar. Air contains approximately 1 mol% argon. Given argon and oxygen adsorb in a similar manner on LiLSX, argon can be lumped with oxygen to form the one effective component referred to as oxygen.[34] Hence, product purity measured experimentally must reflect the additional contribution from argon.

(ii) End of step pressures, reported in kPa. These values were measured directly from transducers located around the RPSA pilot plant at CSS.

Once an operating regime has been established and CSS achieved, a large volume of data can be obtained. In this study, a select number of these parameters will be of primary interest when comparing numerical results against experimental data. In addition to pressure and temperature profiles obtained within the adsorption column, these additional data include:

(i) Total mole flow obtained in the exhaust lines during counter-current depressurization and purge, reported in units of gmole $cycle^{-1}$.

$$\text{Exhaust flow, step } m = \frac{p_A}{RT_A} \times (\text{Gas volume out of exhaust line, step } m) \quad (10)$$

(ii) Total flow in the product line, reported in units of gmole $cycle^{-1}$.

$$\text{Total product flow} = \frac{p_A}{RT_A} \times (\text{Gas volume out of product line over cycle}) \quad (11)$$

(iii) Recovery of oxygen (plus argon) in the product line, reported as a percentage. Note the total flow of oxygen fed into the process is found by adding the total flow of gas obtained in the product and exhaust lines.

$$\text{Recovery} = \frac{100 \times (\text{Total product flow}) \times (O_2 + \text{Ar composition as a \%})}{22 \times \frac{p_A}{RT_A} \times (\text{Gas volume out of exhaust and product lines over cycle})} \quad (12)$$

(iv) The amount of oxygen (plus argon) obtained from the process per unit mass of sorbent per day, denoted specific productivity with units of (kg O_2+Ar) kg^{-1} day^{-1}.

$$\text{Specific productivity} = \frac{27.65 \times (\text{Total product flow}) \times (O_2 + \text{Ar composition as a \%})}{m_{bed} \times t_{cycle}} \quad (13)$$

p_A and T_A represent atmospheric pressure in Pa and temperature in K, respectively. Gas volume out of the product line over a cycle was measured using a dry test meter (DTM) and soap bubble flow meter on the product line, while gas volume out of exhaust line over cycle was measured using an annubar-DP cell arrangement. The mass of LiLSX pellets added to the adsorption column, m_{bed}, was 11.29 ± 0.05 kg. This batch of sorbent was regenerated for 8 h at 733 K in a furnace that was continuously purged with dry air.

With the experimental arrangement of the RPSA pilot plant fully represented numerically, a comparison with experimental data can be made and the merits of the different mass transfer models and their ability to capture process effects assessed. Results for the 400:120 kPa pressure range are denoted RPSA runs 1 through 9, and the conditions are summarized in Table 5.

Experimental data presented in Table 5 (as well as the corresponding comparisons with simulation in Table 6) represent average values obtained over 10 cycles of data acquisition at CSS. The corresponding plus-minus value represents 95% confidence limits on the reported average. In situations where the plus-minus value is smaller than experimental error, experimental error is reported as the 95% confidence limit. Table 5 presents two values for purity; the first represents average purity that was experimentally obtained from the paramagnetic oxygen analyzer over 10 cycles, and the second (in brackets) represents product purity when oxygen and argon are lumped together as the one component. The LDFP model is evaluated using the Alpay and Scott[35] analytical result for the dimensionless parameter K_i. Table 2 reveals θ_i is greater than 0.1 across each cycle time, so $K_i = \pi^2$ for all runs that use the LDFP model. Having presented parameters that define the operating conditions from each of the 9 RPSA runs, the set of results presented in Table 6 compares experimental results for the parameters of interest to their corresponding numerical predictions.

Tables 5 and 6 reveal that 9 of a possible 10 combinations for product purity and cycle time have been covered (see Tables 1 and 2 for all possible combinations). The high purity run, 90 mol%O_2, at the shortest cycle time, t_{cycle} = 8 s, could not be achieved on the RPSA pilot plant without fully closing the product line modulating valve and letting the plant undergo internal purge. Even at this extreme limit, 24 h of continuous operation with a small amount of product gas being withdrawn for purity measurement could barely achieve 87 mol%O_2 under the 400:120 kPa pressure window. Therefore, total cycle time somewhere between 8 and 14 s represents the limiting value of t_{cycle} on the RPSA pilot plant that could maintain separation performance with a finite quantity of product gas being withdrawn per cycle at high purity. This operating constraint means one RPSA run for the 400:120 kPa pressure window has not been considered in this analysis in relation to a product purity of 90 mol%O_2 and cycle time of 8 s.

Error margins for specific productivity reported in Table 6 are based on the ability to measure product flow using the DTM and soap bubble flow meters under steady conditions and, hence, these errors are relatively small. On the other hand, recovery had to be inferred from the accumulated moles of gas obtained in the product and exhaust lines. At short cycle times, the annubar-DP cell arrangement used to measure flow on the exhaust line struggled to capture the flow "spike" that occurs when the column depressurizes to atmosphere and, consequently, underestimates gas volume. The upper part of the error band on RPSA runs 7, 8, and 9, therefore, represents exhaust volume measured experimentally, while the lower part of the error bar represents exhaust volume obtained using the simulator with the DPM activated. Product volume obtained experimentally is used in both of these calculations according to Eq. 11. The actual data point ascribed to the short cycle time represents experimentally measured recovery and, hence, sits at the top of the error bar. This also explains why two values are presented for recovery instead of a plus-minus error on RPSA runs 7, 8, and 9 in Table 6.

The assignment of these two values is discussed later with reference to error bars on the graphical presentation of these data. To assist in the following discussion, four graphs are presented that compare specific productivity and recovery as a function of cycle time from the RPSA pilot plant and simulator, Figures 2a, 2b, 3a, and 3b. In addition, "ideal" lines have been

Table 5. Summary of Experimentally Obtained Step Times, Product Purity, and End of Step Product Tank Pressures That Identify the Operating Conditions for Each RPSA Run

Parameter	RPSA Run 1	RPSA Run 2
Step 1 time (s)	11.3 ± 0.1	11.1 ± 0.1
Total cycle time (s)†	50.0 ± 0.1	50.0 ± 0.1
Product purity (mol%O_2)#	90.0 ± 0.5 (94.0)‡	79.1 ± 0.5 (82.6)‡
Feed temperature (K)*	287.9 ± 0.6	286.5 ± 0.9
T_A (K)	288.7 ± 0.5	287.7 ± 0.5
p_A (kPa)	101.5 ± 0.1	101.8 ± 0.1
p^{tank} end step 1 (kPa)	341 ± 4	333 ± 5
p^{tank} end step 2 (kPa)	398 ± 3	397 ± 3
p^{tank} end step 3 (kPa)	387 ± 3	385 ± 3
p^{tank} end step 4 (kPa)	344 ± 5	336 ± 6

Parameter	RPSA Run 3	RPSA Run 4
Step 1 time (s)	7.3 ± 0.1	8.0 ± 0.1
Total cycle time (s)†	36.0 ± 0.1	36.0 ± 0.1
Product purity (mol%O_2)#	89.2 ± 0.5 (93.2)‡	80.1 ± 0.5 (83.7)‡
Feed temperature (K)*	286.4 ± 0.6	284.7 ± 0.6
T_A (K)	287.7 ± 0.5	285.7 ± 0.5
p_A (kPa)	99.9 ± 0.1	100.8 ± 0.1
p^{tank} end step 1 (kPa)	322 ± 3	325 ± 3
p^{tank} end step 2 (kPa)	391 ± 3	395 ± 3
p^{tank} end step 3 (kPa)	381 ± 3	384 ± 3
p^{tank} end step 4 (kPa)	327 ± 3	328 ± 3

Parameter	RPSA Run 5	RPSA Run 6
Step 1 time (s)	4.2 ± 0.1	4.0 ± 0.1
Total cycle time (s)†	22.0 ± 0.1	22.0 ± 0.1
Product purity (mol%O_2)#	89.3 ± 0.5 (93.3)‡	80.7 ± 0.5 (84.3)‡
Feed temperature (K)*	289.2 ± 1.3	287.8 ± 0.6
T_A (K)	290.2 ± 0.5	288.3 ± 0.5
p_A (kPa)	101.2 ± 0.1	101.1 ± 0.1
p^{tank} end step 1 (kPa)	328 ± 3	320 ± 3
p^{tank} end step 2 (kPa)	393 ± 3	393 ± 3
p^{tank} end step 3 (kPa)	383 ± 3	383 ± 3
p^{tank} end step 4 (kPa)	334 ± 3	328 ± 3

Parameter	RPSA Run 7	RPSA Run 8
Step 1 time (s)	2.7 ± 0.1	2.6 ± 0.1
Total cycle time (s)†	14.0 ± 0.1	14.0 ± 0.1
Product purity (mol%O_2)#	89.8 ± 0.5 (93.8)‡	80.4 ± 0.5 (84.0)‡
Feed temperature (K)*	288.3 ± 0.8	288.4 ± 0.6
T_A (K)	288.2 ± 0.5	289.6 ± 0.5
p_A (kPa)	101.6 ± 0.1	100.3 ± 0.1
p^{tank} end step 1 (kPa)	318 ± 3	309 ± 3
p^{tank} end step 2 (kPa)	391 ± 3	389 ± 3
p^{tank} end step 3 (kPa)	386 ± 3	382 ± 3
p^{tank} end step 4 (kPa)	327 ± 3	320 ± 3

Parameter	RPSA Run 9
Step 1 time (s)	1.5 ± 0.1
Total cycle time (s)†	8.0 ± 0.1
Product purity (mol%O_2)#	80.0 ± 0.5 (83.6)‡
Feed temperature (K)*	290.8 ± 0.5
T_A (K)	290.8 ± 0.5
p_A (kPa)	100.8 ± 0.1
p^{tank} end step 1 (kPa)	297 ± 3
p^{tank} end step 2 (kPa)	376 ± 3
p^{tank} end step 3 (kPa)	376 ± 3
p^{tank} end step 4 (kPa)	314 ± 3

†Step 2 time = Cycle time − Step 1 time − Step 3 time − Step 4 time (see Table 2 for Step 3 time and Step 4 time).
‡The number in brackets represents the adjusted purity mol%O_2 + Ar used for simulation.
#Denotes a parameter that is controlled according to Table 1.
*Feed temperature represents the average temperature of gas passed into the bed over the cycle at CSS. The plus-minus value represents 95% confidence limits on feed temperature.

included that apply the scaling rules of Rota and Wankat[36] for a non-isothermal PSA process that is mass transfer limited at the intrapellet level. Rota and Wankat[36] imposed the LDF model as the governing equation that describes intrapellet mass transfer and set $(\text{Purity})_{\text{current cycle time}} = (\text{Purity})_{\text{cycle time = 50 s}}$ and $(\text{Recovery})_{\text{current cycle time}} = (\text{Recovery})_{\text{cycle time = 50 s}}$ with other bed parameters held constant to produce the following scaling rule:

$$\frac{(\text{Specific productivity})_{\text{current cycle time}}}{(\text{Specific productivity})_{\text{cycle time=50 s}}} = \left(\frac{t_{\text{cycle}}}{50}\right)^{-1} \tag{14}$$

Although purity was controlled experimentally and numerically to one value as a function of cycle time, recovery at $t_{cycle} = 50$ s does not necessarily equal the recovery at a shorter cycle time. For this reason, a deviation in the dependence of specific productivity with $(1/t_{cycle})$ will become evident as the dependence on intrapellet mass transfer and interpellet pressure drop deviates from the Rota and Wankat[36] assumption.

Errors of around 10% between simulated and experimental data are evident at the long cycle time of RPSA run 1, where deviations due to the selected mass-transfer model are minimal. Further examination of this result reveals small deviations in the predicted equilibrium isotherm results in errors on this order of magnitude, particularly when extending pure component equilibrium adsorption data to multicomponent data using Ideal Adsorbed Solution Theory.[19,37]

Comparison of mass transfer models

Accumulated moles of gas obtained in the exhaust line with the DPM and the LDFP model are within 5% of the same value measured experimentally at the long and intermediate cycle times (that is, $t_{cycle} > 14$ s). For RPSA runs where t_{cycle} was 14 s or less, deviations of 5-11% arose between predicted and experimentally observed exhaust gas flows during step 3. Flow spikes at the start of step 3 are very difficult to capture, and the experimental value in Table 6 would be expected to underestimate the actual moles of gas obtained from the column during step 3. Exhaust flow calculated during purge, step 4, is within 11% of numerical predictions using the DPM and LDFP model across all cycle times. During purge the flow of gas leaving the bed is relatively steady such that flow transients that arose just a few seconds earlier have subsided enough to allow a reliable estimate of accumulated moles to be obtained.

Accumulated moles of gas obtained during purge and counter-current depressurization for long cycle times are similar in magnitude to experimental data. However, the moles of gas obtained in the product line show consistently different trends between the DPM and LDFP model. For the DPM, total product flow is consistently overestimated by approximately 20% across all cycle times. The LDFP model overestimates total product flow by 20% at the long cycle time, but once t_{cycle} is 14 s or less, underestimates total product flow by as much as 60%. This result shows the two intrapellet mass-transfer models predict significantly different gas flows out of the top of the bed at the RPSA limit, with the DPM consistently overestimating total product flow in comparison to the LDFP model.

Figures 2 and 3 are presented to discuss trends in specific productivity and recovery obtained numerically and experi-

Table 6. Comparing Experimental and Numerical Parameters from Each RPSA Run

RPSA Run 1 (t_{cycle} = 50 s at 90.0 mol%O_2) Parameter	RPSA Pilot Plant	Simulated	
		LDFP	DPM
p^{bottom} end step 1 (kPa)	343 ± 4	342	343
p^{top} end step 1 (kPa)	342 ± 4	341	342
p^{bottom} end step 2 (kPa)#	400 ± 3	400	401
p^{top} end step 2 (kPa)	399 ± 3	399	400
p^{bottom} end step 3 (kPa)#	121 ± 3	122	121
p^{top} end step 3 (kPa)	122 ± 3	122	122
p^{bottom} end step 4 (kPa)#	140 ± 4	140	139
p^{top} end step 4 (kPa)	142 ± 4	142	142
Exhaust flow step 3 (gmole cycle^{-1})	7.09 ± 0.06	7.35	7.39
Exhaust flow step 4 (gmole cycle^{-1})	1.16 ± 0.06	1.19	1.14
Total product flow (gmole cycle^{-1})	0.410 ± 0.020	0.492	0.507
Recovery (%O_2 + Ar)	20.0 ± 0.8	23.2	24.2
Specific productivity ((kg O_2 + Ar) kg^{-1} day^{-1})	1.89 ± 0.06	2.26	2.33

RPSA Run 2 (t_{cycle} = 50 s at 79.1 mol%O_2) Parameter	RPSA Pilot Plant	Simulated	
		LDFP	DPM
p^{bottom} end step 1 (kPa)	335 ± 5	335	333
p^{top} end step 1 (kPa)	333 ± 5	334	332
p^{bottom} end step 2 (kPa)#	400 ± 3	400	400
p^{top} end step 2 (kPa)	399 ± 3	399	399
p^{bottom} end step 3 (kPa)#	121 ± 3	121	121
p^{top} end step 3 (kPa)	122 ± 3	122	122
p^{bottom} end step 4 (kPa)#	140 ± 5	140	140
p^{top} end step 4 (kPa)	143 ± 5	143	143
Exhaust flow step 3 (gmole cycle^{-1})	7.10 ± 0.06	7.23	7.27
Exhaust flow step 4 (gmole cycle^{-1})	1.16 ± 0.06	1.17	1.15
Total product flow (gmole cycle^{-1})	0.490 ± 0.020	0.611	0.627
Recovery (%O_2 + Ar)	20.8 ± 0.8	25.5	26.0
Specific productivity ((kg O_2 + Ar) kg^{-1} day^{-1})	1.98 ± 0.06	2.47	2.54

RPSA Run 3 (t_{cycle} = 36 s at 89.2 mol%O_2) Parameter	RPSA Pilot Plant	Simulated	
		LDFP	DPM
p^{bottom} end step 1 (kPa)	325 ± 3	323	325
p^{top} end step 1 (kPa)	322 ± 3	321	323
p^{bottom} end step 2 (kPa)#	400 ± 3	401	400
p^{top} end step 2 (kPa)	398 ± 3	400	399
p^{bottom} end step 3 (kPa)#	118 ± 3	119	117
p^{top} end step 3 (kPa)	119 ± 3	121	119
p^{bottom} end step 4 (kPa)#	141 ± 3	140	140
p^{top} end step 4 (kPa)	145 ± 3	145	145
Exhaust flow step 3 (gmole cycle^{-1})	7.23 ± 0.06	7.44	7.52
Exhaust flow step 4 (gmole cycle^{-1})	1.39 ± 0.06	1.53	1.50
Total product flow (gmole cycle^{-1})	0.474 ± 0.020	0.547	0.636
Recovery (%O_2 + Ar)	21.8 ± 0.9	24.3	27.8
Specific productivity ((kg O_2 + Ar) kg^{-1} day^{-1})	3.00 ± 0.07	3.46	4.03

RPSA Run 4 (t_{cycle} = 36 s at 80.1 mol%O_2) Parameter	RPSA Pilot Plant	Simulated	
		LDFP	DPM
p^{bottom} end step 1 (kPa)	328 ± 3	327	326
p^{top} end step 1 (kPa)	326 ± 3	325	324
p^{bottom} end step 2 (kPa)#	400 ± 3	401	401
p^{top} end step 2 (kPa)	398 ± 3	400	400
p^{bottom} end step 3 (kPa)#	122 ± 3	122	121
p^{top} end step 3 (kPa)	123 ± 3	124	123
p^{bottom} end step 4 (kPa)#	140 ± 3	141	140
p^{top} end step 4 (kPa)	144 ± 3	145	144
Exhaust flow step 3 (gmole cycle^{-1})	7.01 ± 0.06	7.19	7.27
Exhaust flow step 4 (gmole cycle^{-1})	1.38 ± 0.06	1.46	1.42
Total product flow (gmole cycle^{-1})	0.516 ± 0.020	0.596	0.639
Recovery (%O_2 + Ar)	21.8 ± 0.8	24.6	26.0
Specific productivity ((kg O_2 + Ar) kg^{-1} day^{-1})	2.94 ± 0.06	3.41	3.64
p^{bottom} end step 1 (kPa)	332 ± 3	332	331
p^{top} end step 1 (kPa)	328 ± 3	328	327
p^{bottom} end step 2 (kPa)#	400 ± 3	401	400
p^{top} end step 2 (kPa)	398 ± 3	399	398
p^{bottom} end step 3 (kPa)#	121 ± 3	121	122
p^{top} end step 3 (kPa)	124 ± 3	124	124
p^{bottom} end step 4 (kPa)#	141 ± 3	141	141

Table 6. Continued

RPSA Run 5 (t_{cycle} = 22 s at 89.3 mol%O_2) Parameter	RPSA Pilot Plant	Simulated LDFP	Simulated DPM
p^{top} end step 4 (kPa)	150 ± 3	149	149
Exhaust flow step 3 (gmole cycle^{-1})	6.97 ± 0.06	7.15	7.30
Exhaust flow step 4 (gmole cycle^{-1})	1.30 ± 0.06	1.43	1.40
Total product flow (gmole cycle^{-1})	0.415 ± 0.020	0.387	0.515
Recovery (%O_2 + Ar)	20.0 ± 0.9	18.3	23.6
Specific productivity ((kg O_2 + Ar) kg^{-1} day^{-1})	4.32 ± 0.11	4.02	5.35

RPSA Run 6 (t_{cycle} = 22 s at 80.7 mol%O_2) Parameter	RPSA Pilot Plant	Simulated LDFP	Simulated DPM
p^{bottom} end step 1 (kPa)	326 ± 3	324	325
p^{top} end step 1 (kPa)	321 ± 3	320	320
p^{bottom} end step 2 (kPa)#	401 ± 3	402	402
p^{top} end step 2 (kPa)	399 ± 3	400	400
p^{bottom} end step 3 (kPa)#	121 ± 3	121	121
p^{top} end step 3 (kPa)	123 ± 3	123	123
p^{bottom} end step 4 (kPa)#	141 ± 3	141	141
p^{top} end step 4 (kPa)	150 ± 3	149	149
Exhaust flow step 3 (gmole cycle^{-1})	6.95 ± 0.06	7.18	7.29
Exhaust flow step 4 (gmole cycle^{-1})	1.28 ± 0.06	1.44	1.39
Total product flow (gmole cycle^{-1})	0.500 ± 0.020	0.535	0.627
Recovery (%O_2 + Ar)	21.7 ± 0.8	22.4	25.8
Specific productivity ((kg O_2 + Ar) kg^{-1} day^{-1})	4.70 ± 0.12	5.02	5.89

RPSA Run 7 (t_{cycle} = 14 s at 89.8 mol%O_2) Parameter	RPSA Pilot Plant	Simulated LDFP	Simulated DPM
p^{bottom} end step 1 (kPa)	327 ± 3	323	324
p^{top} end step 1 (kPa)	318 ± 3	317	317
p^{bottom} end step 2 (kPa)#	402 ± 3	402	402
p^{top} end step 2 (kPa)	397 ± 3	398	398
p^{bottom} end step 3 (kPa)#	121 ± 3	121	122
p^{top} end step 3 (kPa)	127 ± 3	125	127
p^{bottom} end step 4 (kPa)#	142 ± 3	142	142
p^{top} end step 4 (kPa)	164 ± 3	158	158
Exhaust flow step 3 (gmole cycle^{-1})	6.41 ± 0.18	6.60	7.06
Exhaust flow step 4 (gmole cycle^{-1})	1.38 ± 0.06	1.45	1.46
Total product flow (gmole cycle^{-1})	0.327 ± 0.020	0.199	0.397
Recovery (%O_2 + Ar)	15.6 to 17.0	10.3	18.9
Specific productivity ((kg O_2 + Ar) kg^{-1} day^{-1})	5.37 ± 0.17	3.26	6.51

RPSA Run 8 (t_{cycle} = 14 s at 80.4 mol%O_2) Parameter	RPSA Pilot Plant	Simulated LDFP	Simulated DPM
p^{bottom} end step 1 (kPa)	319 ± 3	317	317
p^{top} end step 1 (kPa)	310 ± 3	310	308
p^{bottom} end step 2 (kPa)#	401 ± 3	401	401
p^{top} end step 2 (kPa)	395 ± 3	397	396
p^{bottom} end step 3 (kPa)#	120 ± 3	120	121
p^{top} end step 3 (kPa)	126 ± 3	125	126
p^{bottom} end step 4 (kPa)#	140 ± 3	140	141
p^{top} end step 4 (kPa)	162 ± 3	157	158
Exhaust flow step 3 (gmole cycle^{-1})	6.38 ± 0.10	6.87	7.14
Exhaust flow step 4 (gmole cycle^{-1})	1.36 ± 0.06	1.51	1.48
Total product flow (gmole cycle^{-1})	0.462 ± 0.020	0.379	0.565
Recovery (%O_2 + Ar)	19.2 to 21.3	16.5	23.4
Specific productivity ((kg O_2 + Ar) kg^{-1} day^{-1})	6.79 ± 0.16	5.57	8.29
p^{bottom} end step 1 (kPa)	318 ± 3	309	313
p^{top} end step 1 (kPa)	298 ± 3	297	297
p^{bottom} end step 2 (kPa)#	398 ± 3	398	397
p^{top} end step 2 (kPa)	380 ± 3	389	387
p^{bottom} end step 3 (kPa)#	120 ± 3	121	121
p^{top} end step 3 (kPa)	135 ± 3	130	131
p^{bottom} end step 4 (kPa)#	139 ± 3	139	139
p^{top} end step 4 (kPa)	200 ± 3	176	176
Exhaust flow step 3 (gmole cycle^{-1})	4.97 ± 0.20	5.85	6.47
Exhaust flow step 4 (gmole cycle^{-1})	1.27 ± 0.06	1.09	1.09
Total product flow (gmole cycle^{-1})	0.263 ± 0.020	0.114	0.338
Recovery (%O_2 + Ar)	12.6 to 15.2	6.09	16.2
Specific productivity ((kg O_2 + Ar) kg^{-1} day^{-1})	6.77 ± 0.25	2.91	8.67

#Denotes a parameter that is controlled according to Table 1.

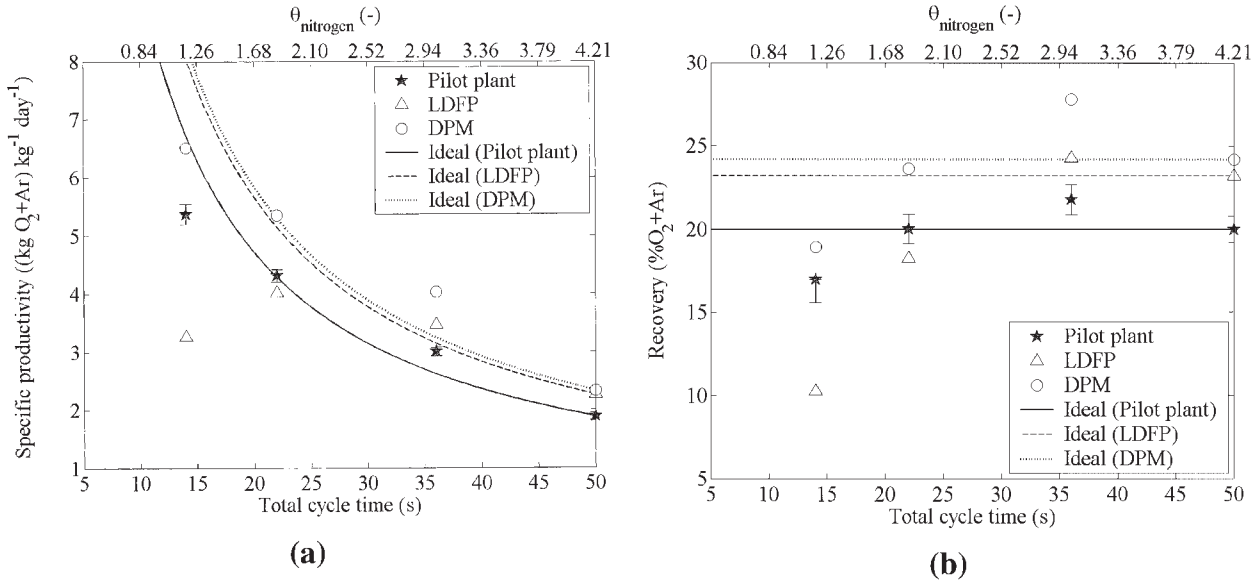

Figure 2. Comparing process performance results between the RPSA pilot-plant data and numerical simulator at a target purity of 90 mol%O_2 for (a) specific productivity and (b) recovery.

mentally from RPSA runs 1 through 9. The first set of results at 90 mol%O_2, Figure 2, shows specific productivity and recovery actually increase above the ideal line both experimentally and numerically when cycle time decreased from 50 to 36 s. A significant change in the role of intrapellet mass transfer and interpellet pressure drop from 50 to 36 s would not be expected, as θ_i was greater than 1 for nitrogen and oxygen from Table 2 and end of step pressures are similar across RPSA runs 1 and 3. While the assumption of working selectivity being independent of any changes to mass transfer and pressure drop appears suitable at these cycle times, the effect of maintaining 140 kPa for end of step purge pressure may have had a very different impact. This suggests the bed may have been over-purged at 50 s with end of step purge pressure set to 140 kPa, whereas 140 kPa was closer to the optimum end of step purge pressure at t_{cycle} = 36 s. At the shortest cycle time, the LDFP model is less than one half of the ideal specific productivity, whereas the DPM and RPSA pilot plant have both decreased by approximately 20% from the ideal line. Given the DPM is in good qualitative agreement with respect to deviations observed from the ideal line with respect to the RPSA pilot plant highlights the fact that the LDFP model has overemphasized the impact of intrapellet mass transfer resistance at cycle times approaching the RPSA limit.

Trends observed at the lower product purity of 80 mol%O_2, Figure 3, show a different trend to those found at 90 mol%O_2.

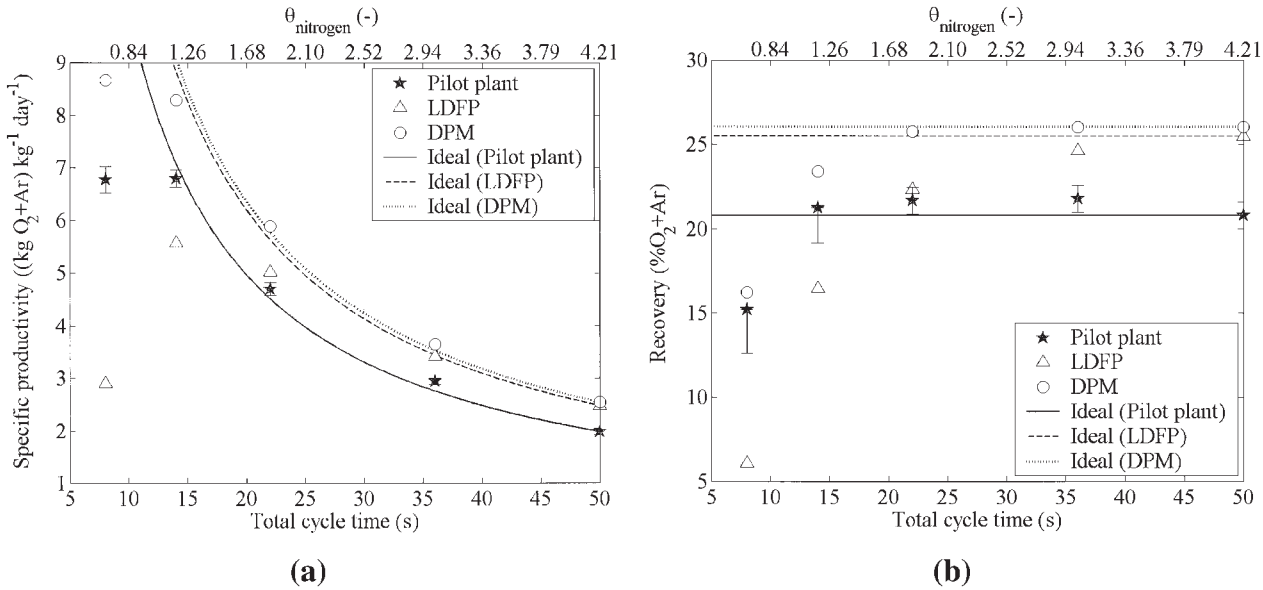

Figure 3. Comparing process performance results between the RPSA pilot-plant data and numerical simulator at a target purity of 80 mol%O_2 for (a) specific productivity and (b) recovery.

Table 7. Simulated Data at CSS for RPSA Run 7 (shortest t_{cycle} at 90 mol%O_2 + Ar) and RPSA Run 9 (shortest t_{cycle} at 80 mol%O_2 + Ar) Under Various Assumptions for Intrapellet Mass Transfer and Interpellet Pressure Drop

RPSA Run 7 (t_{cycle} = 14 s at 89.8 mol%O_2)	Δp^B Finite Using . . .			$\Delta p^B \approx 0$ Using . . .		
Parameter	ILE	LDFP†	DPM‡	ILE	LDFP	DPM
p^{bottom} end step 1 (kPa)	326	323	324	317	317	317
p^{top} end step 1 (kPa)	318	317	317	317	317	317
p^{bottom} end step 2 (kPa)	403	402	402	403	403	403
p^{top} end step 2 (kPa)	399	398	398	403	403	403
p^{bottom} end step 3 (kPa)	121	121	122	122	122	122
p^{top} end step 3 (kPa)	126	125	127	122	122	122
p^{bottom} end step 4 (kPa)	143	142	142	143	142	142
p^{top} end step 4 (kPa)	162	158	158	143	142	142
Exhaust flow step 3 (gmole cycle^{-1})	7.22	6.60	7.06	7.39	6.92	7.42
Exhaust flow step 4 (gmole cycle^{-1})	1.47	1.45	1.46	1.53	1.53	1.55
Total product flow (gmole cycle^{-1})	0.631	0.199	0.397	0.599	0.185	0.398
Recovery (%O_2 + Ar)	28.8	10.3	18.9	26.8	9.10	18.1
Specific productivity ((kg O_2 + Ar) kg^{-1} day^{-1})	10.4	3.26	6.51	9.82	3.03	6.53
RPSA Run 9 (t_{cycle} = 8 s at 80.0 mol%O_2)	Δp^B Finite Using . . .			$\Delta p^B \approx 0$ Using . . .		
Parameter	ILE	LDFP†	DPM‡	ILE	LDFP	DPM
p^{bottom} end step 1 (kPa)	316	309	313	296	296	298
p^{top} end step 1 (kPa)	298	297	297	296	296	298
p^{bottom} end step 2 (kPa)	397	398	397	398	398	398
p^{top} end step 2 (kPa)	385	389	387	398	398	398
p^{bottom} end step 3 (kPa)	121	121	121	121	121	121
p^{top} end step 3 (kPa)	133	130	131	121	121	121
p^{bottom} end step 4 (kPa)	139	139	139	140	139	139
p^{top} end step 4 (kPa)	183	176	176	140	139	139
Exhaust flow step 3 (gmole cycle^{-1})	6.70	5.85	6.47	7.27	6.45	7.20
Exhaust flow step 4 (gmole cycle^{-1})	1.08	1.09	1.09	1.22	1.21	1.23
Total product flow (gmole cycle^{-1})	0.629	0.114	0.338	0.609	0.069	0.334
Recovery (%O_2 + Ar)	28.3	6.09	16.2	25.4	3.38	14.5
Specific productivity ((kg O_2 + Ar) kg^{-1} day^{-1})	16.1	2.91	8.67	15.6	1.76	8.56

†These results have been taken directly from the "LDFP" entries of Table 6.
‡These results have been taken directly from the "DPM" entries of Table 6.

First, a large improvement in specific productivity and recovery above the ideal line is not observed when t_{cycle} decreased from 50 to 22 s with the DPM and RPSA pilot plant. This suggests the relative importance of intrapellet mass transfer, interpellet pressure drop, and end of step purge pressure is not significantly altering working selectivity across these cycle times. The fact that the LDFP model predicts a reduction in specific productivity and recovery from the ideal line at t_{cycle} = 22 s with respect to the RPSA pilot plant and DPM again indicates the LDFP model is overemphasizing the impact of intrapellet mass transfer resistance. Once the shortest cycle time is reached at 80 mol%O_2, the LDFP model is not even in qualitative agreement with the RPSA pilot plant or DPM. The LDFP model at t_{cycle} = 8 s suggests specific productivity is decreasing rapidly, whereas the RPSA pilot plant and DPM indicate specific productivity has reached something close to a local maximum as a function of cycle time.

From this initial discussion, it is evident intrapellet mass transfer resistance is overemphasized within the LDFP model in relation to the DPM and RPSA pilot plant for $t_{cycle} < 30$ s. At cycle times approximately greater than 22 s, it also appears that interpellet pressure drop is of minor importance given the general agreement between end of step pressure profiles. At shorter cycle times, however, end of step pressure changes and the role of interpellet pressure drop may become important. To address this issue of intrapellet mass transfer versus interpellet pressure drop resistance at the RPSA limit, three additional simulations have been performed at the shortest cycle times experimentally achieved for both the 80 and 90 mol%O_2 purities and 400:120 kPa pressure window.

(i) The first of these additional simulations applied Instantaneous Local Equilibrium (ILE) by assigning the LDF constant K_i a value of 1.0×10^{10}. This same simulation did not change any other parameter, so this simulation reflects the RPSA limit in the presence of interpellet pressure drop but no mass transfer resistance.

(ii) The second simulation was performed under conditions where the constants of the pressure drop equation $\kappa_{viscous}$ and $\kappa_{kinetic}$ are two orders of magnitude smaller than their corresponding values obtained experimentally.[18] With all other parameters remaining the same, this simulation reflects the RPSA limit in the presence of mass transfer resistance but no interpellet pressure drop.

(iii) The third run combines cases (i) and (ii) above to simulate conditions in the absence of pressure drop and mass transfer resistance.

Numerical results obtained from the additional simulations performed on RPSA runs 7 and 9 are summarized in Table 7. ILE results with Δp^B finite at both purities show separation performance is significantly higher than the equivalent DPM and LDFP model results. Therefore, intrapellet mass transfer resistance is present at the intrapellet level, and the relative importance of this resistance is overemphasized within the LDFP model. Lu et al.[38] found separation performance pre-

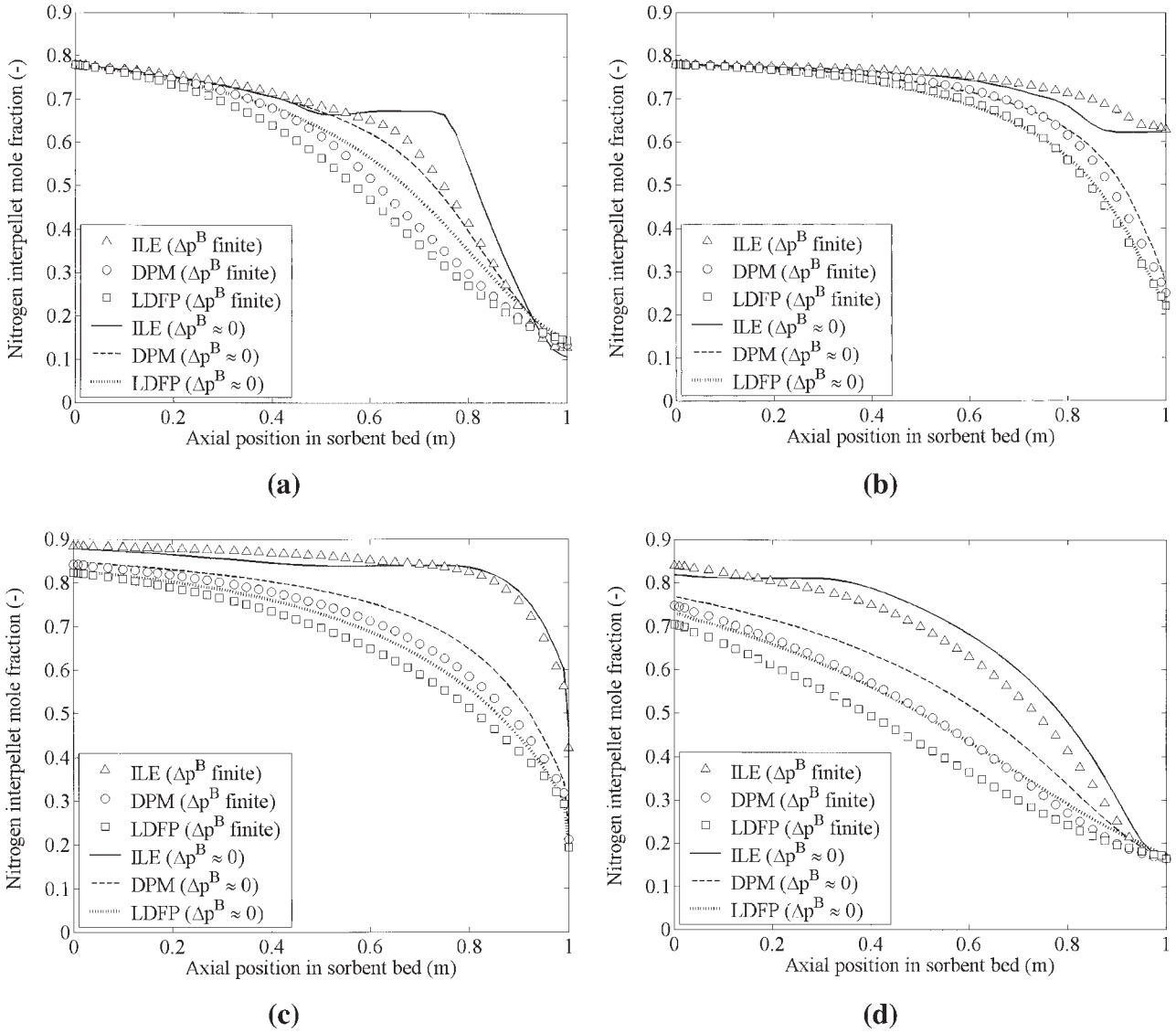

Figure 4. Composition profiles obtained from RPSA run 9 (80.0 mol%O_2) using six different modeling options at the end of step (a) 1, (b) 2, (c) 3, and (d) 4.

dicted from a DPM that incorporates intrapellet viscous flow will fall somewhere between a DPM that incorporates diffusion only and the ILE assumption. Although intrapellet mass transfer is important at the RPSA limit when Δp^B is finite, a rather curious observation from Table 7 is made when $\Delta p^B \approx 0$. Both RPSA runs 7 and 9 show separation performance actually decreased when the ILE assumption, DPM and LDFP model was used using $\Delta p^B \approx 0$. To assist in the following discussion, end of step composition profiles obtained from all modeling options for RPSA run 9 are presented in Figure 4. The trends between RPSA runs 7 and 9 are similar and, hence, RPSA run 7 is omitted for brevity.

During feed pressurization, Figure 4a, the penetration distance of nitrogen increases when $\Delta p^B \approx 0$ with respect to the same simulation using Δp^B finite. Feed pressurization (step 1) terminates and the product line opens (step 2) when the pressure in the top void matches product tank pressure. For the simulation where $\Delta p^B \approx 0$, the entire bed is effectively at tank pressure, whereas bed pressure is higher, on average, with Δp^B finite as bottom void pressure is greater than top void pressure (see p^{bottom} and p^{top} entries in Table 7 for step 1). The capacity for nitrogen adsorption across the bed is slightly higher with Δp^B finite and, hence, a larger portion of feed gas is adsorbed, allowing the nitrogen front to be held further back in the bed. By the end of step 2, the axial pressure gradient is relatively flat, and the final shape of the composition profile is similar between Δp^B finite and $\Delta p^B \approx 0$ to maintain product purity. The reason for specific productivity and recovery being slightly lower with $\Delta p^B \approx 0$ can be largely attributed to this difference in working capacity for nitrogen adsorption between steps 1 and 2 than any intrinsic influence from the presence of intrapellet mass transfer alone.

Nitrogen composition is similar at the end of step 2 whether Δp^B is finite or $\Delta p^B \approx 0$ (Figure 4b) given the role of intrapellet mass transfer does not significantly change between these runs. A similar observation is also made for nitrogen composition by

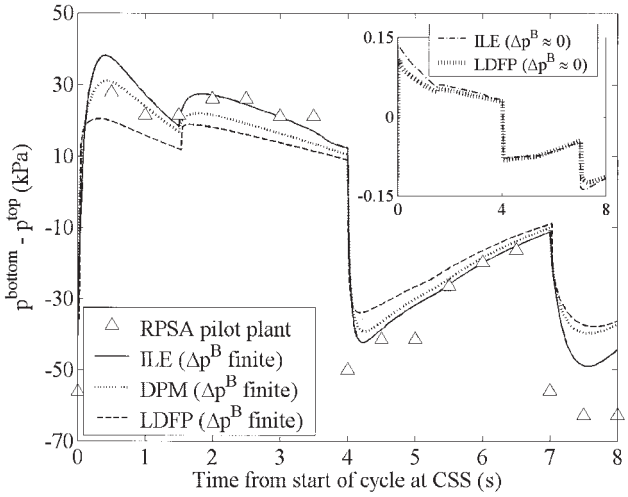

Figure 5. Magnitude of the pressure gradient across the sorbent bed obtained experimentally and numerically under various modeling assumptions for RPSA run 9.

The inlay graph provides a visual guide only to the magnitude of the numerical pressure gradient that arose for simulations where $\Delta p^B \approx 0$. DPM lines for $\Delta p^B \approx 0$ are not shown for brevity but lie between the ILE and LDFP lines on the inlay graph.

the end of counter-current depressurization, step 3. The only noticeable difference between a simulation where Δp^B is finite and $\Delta p^B \approx 0$ for step 3 is the moles of gas exhausted from the bed (Table 7). A simulation where Δp^B is finite produces a pressure gradient from top to bottom that is approximately 6 kPa (RPSA run 7) and 10 kPa (RPSA run 9) in magnitude, which is not significant enough to influence interpellet nitrogen mole fraction in comparison to $\Delta p^B \approx 0$ according to Figure 4c. However, a simulation where Δp^B is finite means the bed, on average, is slightly higher in pressure, so the equivalent simulation where $\Delta p^B \approx 0$ must exhaust a larger volume of gas to achieve end of step pressure. A similar argument reveals purge, step 4, is performed at a higher pressure on average when Δp^B is finite. With purge now performed at a slightly higher pressure when Δp^B is finite, the gas phase is not enriched with desorbed nitrogen to the same extent as when $\Delta p^B \approx 0$.

Overall, the difference in specific productivity and recovery for the three mass-transfer options between Δp^B finite and $\Delta p^B \approx 0$ is not as large as the difference observed between the ILE assumption, DPM and LDFP model when Δp^B is finite. Small differences between the ILE assumption, DPM and LDFP model for Δp^B finite versus $\Delta p^B \approx 0$ could also be rationalized on the basis that nitrogen working capacity between steps 1 and 2 was slightly different and mass transfer had a minor impact on changes in process performance (that is, compare the relative differences in performance between the ILE assumption for Δp^B finite and $\Delta p^B \approx 0$, where no transfer arises, and then for the DPM and LDFP model where mass transfer is important; there is not a big difference in the relative change in performance).

On this basis interpellet pressure drop mainly alters the available working capacity for nitrogen adsorption. One last comparison shall be made using data obtained from the results of Table 7 with respect to RPSA pilot plant data. Applying different assumptions on intrapellet mass transfer using Δp^B finite, in each case, gave rise to an axial pressure gradient across the sorbent bed that was generally in good agreement with RPSA pilot-plant data (Figure 5). The pressure gradient is highest when the bed behaves under ILE conditions, with the pressure gradient subsiding in magnitude progressively as each intrapellet mass transfer model in introduced into the system. Under ILE conditions, the rate of nitrogen adsorption/desorption is highest as the gas can be taken up/released from the pellets instantaneously; therefore, gas flows must be high to achieve the required end of step pressure. With the LDFP model, intrapellet mass transfer is limiting and the bed is partially inert with respect to an ILE run; hence, gas flows do not need to be as high to reach end of step pressure and, consequently, bed pressure drop is lower. Despite small differences in simulated pressure drop, the general trend from RPSA run 9 (Figure 5) is that pressure profiles compare well against experimental data with the exception of the purge step, where the simulator generally underestimates the pressure gradient from top to bottom. Identical trends are observed for RPSA run 7 and are omitted here for brevity.

For each simulation performed in this study, the same values of C_K and C_m used with the VF+DGM, 0.166 and 0.083, respectively, were used in $D^e_{m,ij}$ and $D^e_{K,i}$ for the LDFP model (Table 8 compares the magnitude of each transport coefficient contained within the LDFP and VF+DGM). Although it could be argued that independent values of C_K and C_m should be found for the LDFP model, this statement is not correct given that Fick's first law of diffusion, which underlies the LDFP model, assumes the intrapellet pore network is identical to that imposed on the VF+DGM. In fact, the only difference between the VF+DGM and Fick's first law constitutive equations is the assumption of equimolar counterdiffusion. Volume averaging the pellet using one radial node over the sorbent pellet was required to generate the LDFP model. It should be recalled that both Fick's first law and volume averaging with $N_r = 1$ (in addition to defining an intrapellet profile that leads to the introduction of a time dependent LDF constant K_i) do not alter the general nature of the intrapellet pore network, and tortuosity coefficients should be general to each transport mechanism within the pellets. Viscous flow has a minimal impact on

Table 8. Effective Diffusion Coefficients for Nitrogen and Oxygen in Zeochem LiLSX Over the Range of Operating Conditions Investigated in the RPSA Pilot Plant

Temperature (K)	Pressure (kPA)	D^e_m for N_2–O_2 ($m^2\ s^{-1}$)	D^e_K for N_2 ($m^2\ s^{-1}$)	D^e_K for O_2 ($m^2\ s^{-1}$)	$B^e p^P/\mu_P$ ($m^2\ s^{-1}$)
290	100	3.27×10^{-6}	3.22×10^{-6}	3.02×10^{-6}	6.43×10^{-7}
290	400	8.19×10^{-7}	3.22×10^{-6}	3.02×10^{-6}	2.58×10^{-6}
320	100	3.90×10^{-6}	3.39×10^{-6}	3.17×10^{-6}	6.43×10^{-7}
320	400	9.74×10^{-7}	3.39×10^{-6}	3.17×10^{-6}	2.58×10^{-6}

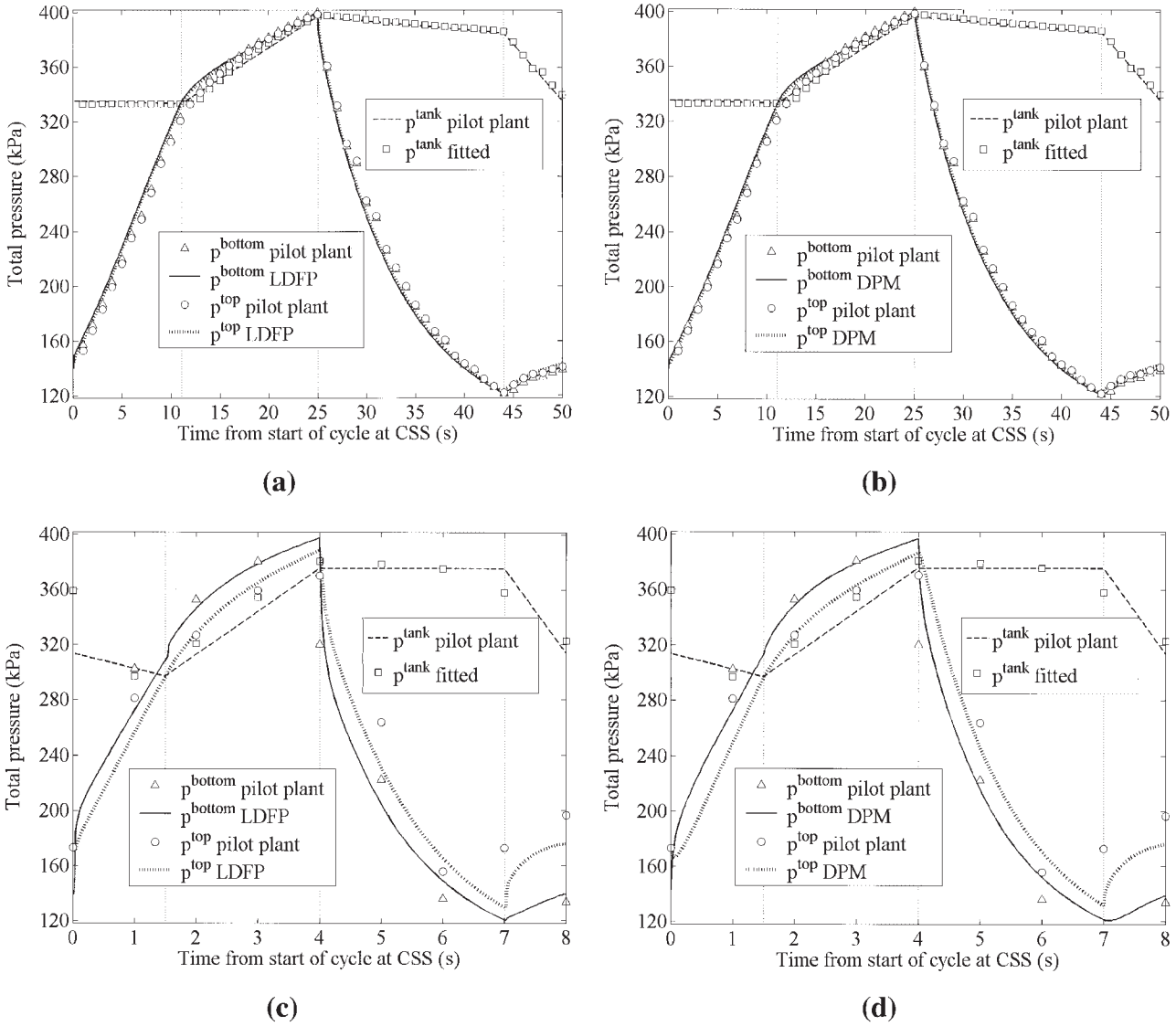

Figure 6. Comparing experimental vs. simulated pressure profiles with time at CSS using both intrapellet mass-transfer models of the simulator.

"p^{tank} pilot plant" represents experimental data and "p^{tank} fitted" linear interpolation of experimental data.
(a) RPSA run 2 with LDFP, (b) RPSA run 2 with DPM, (c) RPSA run 9 with LDFP, and (d) RPSA run 9 with DPM.

intrapellet mass transfer, so the mechanisms of Knudsen and molecular diffusion are dominant; the LDFP model suitably accounts for both of these diffusion mechanisms within a pore network that is assumed equivalent to that imposed on the VF+DGM. The discussion of Todd and Webley[30] found tortuosity coefficients for LiLSX pellets agree well against existing literature estimates, so the magnitude of C_K and C_m should not be all that different from the values found using the VF+DGM. Todd and Webley[15] revealed the assignment of the LDF constant K_i and equimolar counterdiffusion were limiting assumptions at the pellet level as cycle time approaches the RPSA limit; data obtained in this study further reinforce this statement.

The use of a conventional LDF model to simulate an RPSA cycle, from the preceding discussion, indicates a new limiting value for θ_i that is greater than 0.1 should be adopted; a value closer to 1.0 is recommended from this analysis. While the LDFP model failed to predict general trends at cycle times approaching the RPSA limit, transport coefficients obtained from an independent set of KTU and LUB experiments with the VF+DGM approach have captured general trends in RPSA pilot plant data at cycle times approaching the RPSA limit.

Comparison of pressure profiles at CSS

Having addressed process performance as a function of cycle time, we now compare experimental and numerical pressure profiles using both the VF+DGM and LDFP mass transfer models. Two of the nine RPSA runs have been graphically presented in this study (Figures 6a, b, c, and d) as a representative sample of the entire data set. The longest and shortest cycle times are shown. These trends all relate to 80 mol%O_2

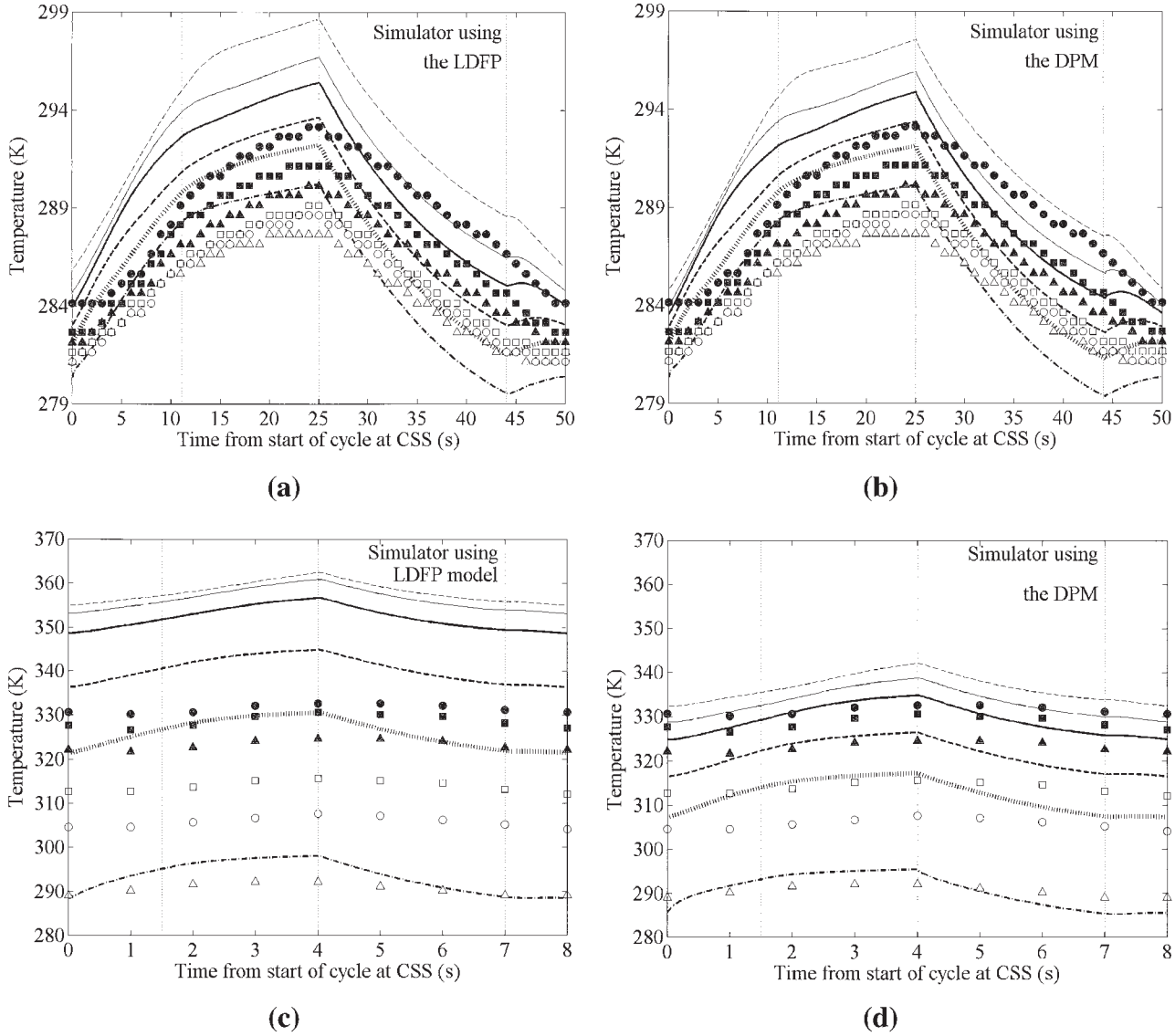

Figure 7. Comparing experimental vs. simulated temperature profiles with time at CSS using both intrapellet mass-transfer models of the simulator.

(a) RPSA run 2 with LDFP, (b) RPSA run 2 with DPM, (c) RPSA run 9 with LDFP, and (d) RPSA run 9 with DPM.

runs. Qualitatively identical profiles are observed for the 90 mol%O_2 RPSA runs and are not shown for brevity.

At cycle times reminiscent of a PSA cycle, t_{cycle} = 50 s, good agreement is seen between experimental and numerical pressure profiles. These results justify the use of void volumes and the compressible valve equation to independently reproduce pressure profiles expected from a typical PSA cycle. Numerical versus experimental predictions show the DPM and LDFP model both reproduce experimental pressure profiles well from the long to short cycle times. On this basis, comparing pressure profiles alone does not reveal any significant deviations between the DPM and LDFP model, in contrast to the trend observed in Figures 2 and 3 in relation to process performance. However, two regions where the DPM and LDFP models do show some discrepancy occur at the start of feed pressurization and counter-current depressurization, steps 1 and 3, respectively, for the short cycle time (Figures 6c and 6d). These observations can be attributed to the rate at which pellets take up/release sorbate molecules from/to the interpellet region using a VF+DGM versus LDFP approach. At short contact times, bulk gas motion and viscous flow (VF+DGM) are crucial components of intrapellet mass transfer with respect to gas entering and leaving a sorbent pellet. The LDFP model, on the other hand, imposes equimolar counterdiffusion on gas transport. During feed pressurization, gas can enter the pellets and be adsorbed much faster using the VF+DGM approach; hence, the interpellet region takes longer to pressurize. During counter-current depressurization, the opposing argument holds, and desorbed gas leaves the pellets much faster (VF+DGM) to replenish the interpellet region. The importance of desorbed gas replenishing the interpellet region was evident between the adsorbing and non-adsorbing conditions for rapid depressurization experiments performed by Todd and Webley.[18] The LDFP model "depletes" and "replenishes" interpellet gas

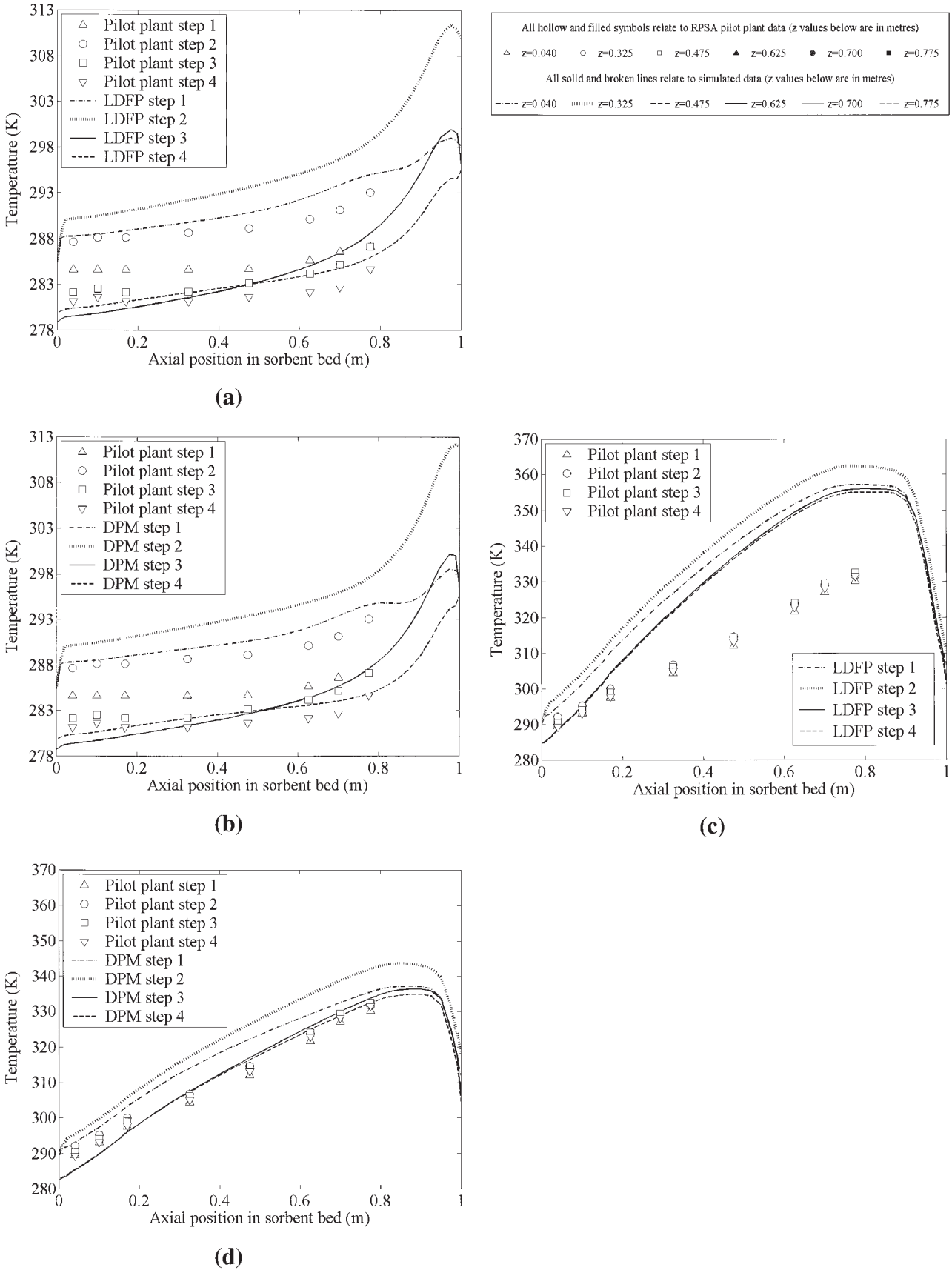

Figure 8. Comparing experimental vs. simulated end of step temperature profiles at CSS using both intrapellet mass-transfer models of the simulator.

(a) RPSA run 2 with LDFP, (b) RPSA run 2 with DPM, (c) RPSA run 9 with LDFP, and (d) RPSA run 9 with DPM.

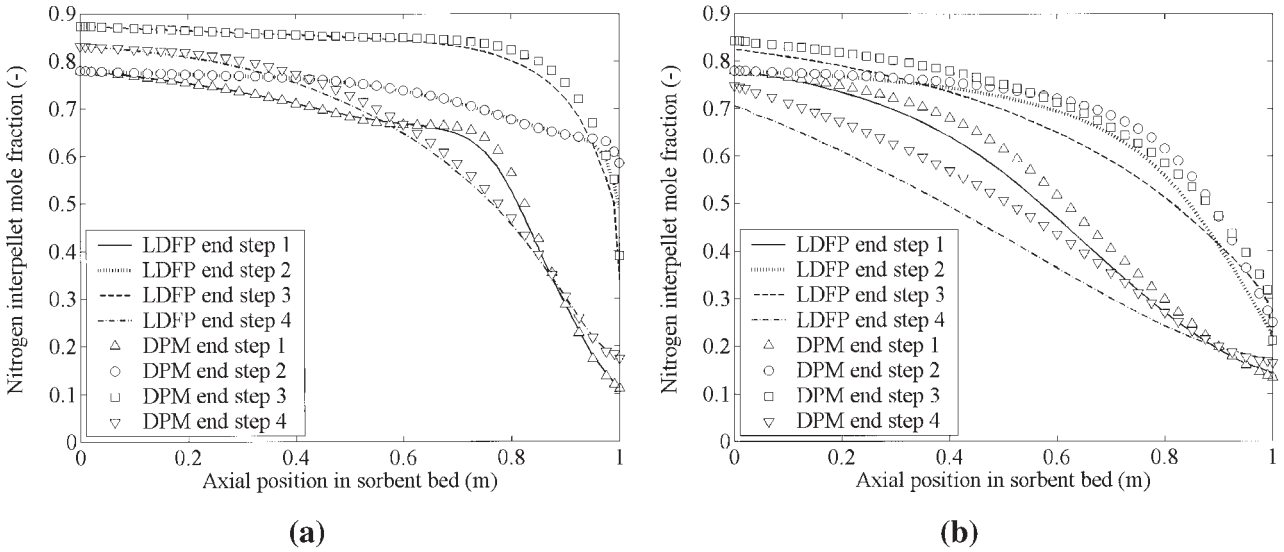

Figure 9. Simulated end of step composition profiles for nitrogen obtained with the DPM and LDFP model from (a) RPSA run 2 and (b) RPSA run 9.

slower than the VF+DGM. Hence, the sorbent bed is almost semi-inert during the early stages of steps 1 and 3, giving rise to a sharp increase and decrease in pressure, respectively. Difficulties in data acquisition at these short time intervals prevent this statement from being experimentally validated.

Figure 6 reveals the largest discrepancy between experimental and numerical pressure resides in the top void region during purge, step 4, at short cycle times. Numerical predictions for p^{top} at the end of step 4 with $t_{cycle} = 14$ s are approximately 5 kPa lower than those from the RPSA pilot plant. At $t_{cycle} = 8$ s, this discrepancy has increased to 20 kPa. Given purge is performed in 1 s when $t_{cycle} = 8$ s, errors in flow geometry simulated between the product tank and sorbent bed interface at $z = L_{bed}$ will be most pronounced. Numerically, the top void is a CSTR that can accumulate a small volume of gas between $z = L_{bed}$ and the product tank. This same region, however, does not provide any pressure drop. On the RPSA pilot plant, the top void comprises several pipe sections with 90° bends, in addition to a filter element that removes entrained adsorbent dust. To purge the bed with pressure increasing from 120 to 140 kPa in 1 s suggests momentum transfer in the top pipe manifold was important in comparison to longer cycle times. Despite this, good qualitative agreement is observed, and the inclusion of a pipe K factor into the upper void CSTR model may assist in closing this mismatch.

Comparison of temperature profiles at CSS

Eight pre-calibrated junction exposed T-type thermocouples were placed in the center of the sorbent bed at different axial locations to measure temperature. The corresponding temperature vs. time graphs for RPSA runs 2 and 9 are shown in Figure 7. Figure 7 shows the simulator predicts a greater temperature change than those experimentally observed. Similar observations were made by Teague and Edgar[10] when comparing their temperature profiles to experimental data. Teague and Edgar[10] proposed this difference was attributed to an "unmodeled temperature gradient within the zeolite pellets." Todd[19] indicates temperature gradients within the pellets would be minimal, even under RPSA conditions, so the explanation appears more likely to be a manifestation of heat transfer resistance between the packed bed and exposed tip of the junction exposed thermocouple. During feed pressurization, numerical temperatures rapidly increase as pressure increases and nitrogen adsorbs. Once the product line opens and gas is withdrawn from the bed, the rate of change of pressure decreases, and so does the rate of change of temperature. For the longest cycle time, $t_{cycle} = 50$ s, this trend over the first two steps of the cycle is loosely observed on the RPSA pilot plant. As cycle time reduces, the experimental transients do not show this distinct change in gradient commonly observed numerically between steps 1 and 2, obviously being a strong function of gas-to-thermocouple heat transfer resistance just mentioned.

For the shortest cycle time, temperature swing predicted numerically at any one point in the bed was smaller than that observed for the longest cycle time. The predicted swing in temperature from both the DPM and LDFP model during RPSA run 2 is approximately 11-12 K (Figures 7a and 7b), while they are approximately 8-9 K during RPSA run 9 (Figures 7c and 7d). Temperature swing observed experimentally for RPSA run 2 is approximately 8-9 K, while the same value was 11-12 K with the DPM and LDFP model.

What does change between the long and short cycle times, however, is the axial temperature gradient across the sorbent bed. Figure 8 compares end of step temperature profiles obtained from the RPSA pilot plant with numerical data. Each graph in Figure 8 is the end of step counterpart to pressure profiles in Figure 6 and temperature profiles in Figure 7. Simulation data at long cycle times show temperature increases rather sharply across the upper regions of the bed. To help explain these results, numerical composition profiles obtained from the DPM and LDFP model from RPSA runs 2 and 9 are useful to consider (see Figure 9). The mole fraction of nitrogen at the end of step 1 from RPSA run 2 (Figure 9a) indicates the bed is similar in composition to air for $z < \approx 0.7$ m. During

step 2 the MTZ moves from $z \approx 0.7$ to $z \approx 1.0$ m, and 100% breakthrough is imminent. A significant amount of nitrogen adsorbs between $0.7 < z < 1.0$ that liberates a large amount of heat in comparison to the rest of the sorbent bed below $z \approx 0.7$ m. This increased amount of nitrogen adsorption explains the sharp increase in numerical bed temperature for axial regions above $z \approx 0.7$ m. Although axial temperature gradient increases sharply above $z \approx 0.7$ m, the actual swing in temperature itself is similar as the entire bed moves from high to low pressure with time (that is, pressure drop is relatively low so working capacity is similar from $z = 0$ to $z = L_{bed}$).

In general, predicted temperature profiles obtained with both the DPM and LDFP model for the long cycle time (Figures 8a and 8b) are in qualitative agreement with experimental trends. Figures 8a and 8b show RPSA pilot-plant temperature is beginning to increase at an axial coordinate similar to that predicted from both the DPM and LDFP model. The other trend evident from Figure 8 is the increase in sorbent bed temperature with axial position as cycle time decreases. At shorter cycle times, interpellet velocity increases to maintain the same pressure window and, consequently, the MTZ broadens. This requires the MTZ to be held further back in the bed to maintain product purity over step 2. To contain the MTZ within the bed, the amount of gas withdrawn from the top of the bed has to decrease, and product recovery drops accordingly. For a system where heat loss to the environment is a small component of the total energy passing through the bed, enthalpy entering the bed at $z = 0$ simply accumulates as less enthalpy is taken out as product. This explains the gradual sharpening of axial temperature profiles across Figure 8 with a reduction in cycle time. The fact that the LDFP model draws less gas out of the bed in relation to the DPM to maintain purity for RPSA runs 9 and 18 means the temperature increases by almost 100 K from feed gas temperature. The DPM allows more gas to exit the bed using a VF+DGM approach and, hence, the temperature is significantly lower, increasing by approximately 60 K from feed conditions The DPM is also in good agreement with experimental temperature profiles at the short cycle time.

Concluding Remarks

Simulation results from both the DPM and LDFP model were similar at long cycle times, indicating the form of the intrapellet mass transfer model under typical PSA conditions is not an important aspect of process simulation to maintain. This was expected. However, numerical results at long cycle times overestimated experimental data, and this was attributed to failure in IAST to correctly predict multicomponent data. As cycle time decreased, the LDFP model failed to match experimental trends in separation performance, predicting recovery and specific productivity will drop due to intrapellet mass transfer resistance at a cycle time higher than the DPM and RPSA pilot plant predicted.

Performing additional simulations at the shortest cycle times experimentally achieved using various assumptions on process operation found the ILE assumption predicted significantly higher production rates and oxygen recovery in comparison to the DPM and LDFP model; hence, intrapellet mass transfer is present at the RPSA limit. This result also indicates the LDFP model provides a conservative estimate of performance, overemphasizing intrapellet mass transfer when approaching the RPSA limit. A second set of simulations reduced interpellet pressure drop to an almost insignificant level for the ILE, DPM and LDFP model. Results from these simulations revealed process operation changed only slightly from the case where pressure drop was finite, and this small change was attributed to the different working capacity of the sorbent bed; intrapellet mass transfer had a minimal impact on process operation between pressure drop finite and the same run where pressure drop is negligible at the RPSA limit.

Using the LDFP model with existing correlations for time adjusted LDF constants does not appear suitable based on the nature of boundary conditions that arise at the pellet surface when approaching the RPSA limit. In order for the LDFP model to correctly match experimental trends at these cycle times, the LDF constant would have to increase before θ_i is 0.1. Independent pellet simulations of Todd and Webley[15] and Todd,[19] in addition to RPSA process simulation performed in this study, indicate the LDF constant would need to begin increasing at a θ_i value closer to 1.

While interpellet pressure profiles obtained from the DPM and LDFP model matched experimental trends across all cycle times, small differences in pressure between the DPM and LDFP model around rapid changes in pressure were attributed to differences in the rate of mass transfer from the intra- to interpellet region and vice versa when bulk gas motion (VF+DGM) is included. Numerical temperature profiles, on the other hand, were found to overestimate experimental profiles due to the slow thermal response of junction-exposed thermocouples within a packed bed. Despite this, end of step temperature at long cycle times was in good qualitative agreement using both the DPM and LDFP model. End of step temperature at short cycle times was generally well predicted with the DPM, and an axial temperature gradient close to 60 K arose. The LDFP model incorrectly predicted this same axial temperature gradient to be almost 100 K.

Acknowledgments

The authors gratefully acknowledge the support of Air Products and Chemicals, Inc., and the Dept. of Chemical Engineering, Monash University.

Literature Cited

1. Ruthven DM. Commentaries. Past progress and future challenges in adsorption research. *Indus Eng Chem Res.* 2000;39:2127-2131.
2. Sircar S. Applications of gas separation by adsorption for the future. *Adsorption Sci Technol.* 2001;19:347-366.
3. Sircar S. Commentaries. Pressure swing adsorption. *Indus Eng Chem Res.* 2002;41:1389-1392.
4. Kulish S, Swank RP. *Rapid Cycle Pressure Swing Adsorption Oxygen Concentration Method and Apparatus*. US Patent No. 5 827 358; October 27, 1998.
5. Keefer BG, McLean CR. *Life Support Oxygen Concentrator*. US Patent No. 6 514 319; February 4, 2003.
6. Turnock PH, Kadlec RH. Separation of nitrogen and methane via periodic adsorption. *AIChE J.* 1971;17:335-342.
7. Jianyu G, Zhenhua Y. Analog circuit for simulation of pressure swing adsorption. *Chem Eng Sci.* 1990;45:3063-3069.
8. Alpay E, Kenney CN, Scott DM. Adsorbent particle size effects in the separation of air by rapid pressure swing adsorption. *Chem Eng Sci.* 1994;49:3059-3075.
9. Suzuki M, Suzuki T, Sakoda A, Izumi J. Piston-driven ultra rapid pressure swing adsorption. *Adsorption.* 1996;2:111-119.
10. Teague KG, Edgar TF. Predictive dynamic model of a small pressure

swing adsorption air separation unit. *Indus Eng Chem Res.* 1999;38: 3761-3775.
11. Arvind R, Farooq S, Ruthven DM. Analysis of a piston PSA process for air separation. *Chem Eng Sci.* 2002;57:419-433.
12. Do DD, Mayfield PLJ. A new simplified model for adsorption in a single particle. *AIChE J.* 1987;33:1397-1400.
13. Serbezov A, Sotirchos SV. Multicomponent transport effects in sorbent particles under pressure swing conditions. *Indus Eng Chem Res.* 1997;36:3002-3012.
14. Serbezov A, Sotirchos SV. Particle-bed model for multicomponent adsorption-based separations: application to pressure swing adsorption. *Chem Eng Sci.* 1999;54:5647-5666.
15. Todd RS, Webley PA. Limitations of the LDF/equimolar counterdiffusion assumption for mass transport within porous adsorbent pellets. *Chem Eng Sci.* 2002;57:4227-4242.
16. Thomas WJ, Crittenden B. *Adsorption Technology and Design.* Street Oxford: Butterworth-Heinemann; 1998:31-32.
17. Ergun S. Fluid flow through packed columns. *Chem Eng Prog.* 1952; 48:89-94.
18. Todd RS, Webley PA. Pressure drop in a packed bed under nonadsorbing and adsorbing conditions. *Indus Eng Chem Res.* 2005;44: 7234-7241.
19. Todd RS. Ph.D. Dissertation. Monash University, Australia, 2003.
20. Doong SJ, Propsner P. Effect of operation symmetry on pressure swing adsorption process. *Adsorption.* 1998;4:149-158.
21. Michael K. Industrial gas: surveying onsite supply options. *Chem Eng.* 1997;January:72-79.
22. Pollard WG, Present RD. On gaseous self-diffusion in long capillary tubes. *Phys Rev.* 1948;73:762-774.
23. Glueckauf E. Theory of chromatography. Part 10. Formulae for diffusion into spheres and their application to chromatography. *Trans Faraday Soc.* 1955;51:1540-1551.
24. Jury SH. An improved version of the rate equation for molecular diffusion in a dispersed phase. *AIChE J.* 1967;13:1124-1126.
25. Nakao SI, Suzuki M. Mass transfer coefficient in cyclic adsorption and desorption. *J Chem Eng* Japan. 1983;16:114-119.
26. Dangieri TJ, Cassidy RT. *RPSA Process*. U.S. Patent No. 4 406 675; September 27, 1983. lt lt
27. Wells AA. *Pressure Swing Gas Separation*. U.S. Patent No. 5 069 688; December 3, 1991.
28. Ruthven DM. *Principles of Adsorption and Adsorption Processes*. New York: John Wiley and Sons, Inc.; 1984:214.
29. Todd RS, Webley PA, Whitley RD, LaBuda MJ. Knudsen diffusion and viscous flow dusty-gas coefficients for pelletised zeolites from kinetic uptake experiments. *Adsorption.* 2005;11:427-432.
30. Todd RS, Webley PA. Macropore diffusion dusty-gas coefficient for pelletised zeolites from breakthrough experiments in the O_2/N_2 system. *Chem Eng Sci.* 2005;60:4593-4608.
31. Todd RS, He J, Webley PA, Beh C, Wilson S, Lloyd MA. Fast finite-volume method for PSA/VSA cycle simulations—experimental validation. *Ind Eng Chem Res.* 2001;40:3217-3224.
32. Webley PA, He J. Fast solution-adaptive finite volume method for PSA/VSA cycle simulation; 1 single step simulation. *Computers Chem Eng.* 2000;23:1701-1712.
33. Marlin TE. *Process Control: Designing Processes and Control Systems for Dynamic Performance*. Singapore: McGraw-Hill; 1995:266-270.
34. Chou CT, Chen LH. Ternary component simulation of a pressure swing adsorption process for air separation. *J Chin Inst Chem Eng.* 1994;25:361-365.
35. Alpay E, Scott DM. The linear driving force model for fast-cycle adsorption and desorption in a spherical particle. *Chem Eng Sci.* 1992;47:499-502.
36. Rota R, Wankat PC. Intensification of pressure swing adsorption processes. *AIChE J.* 1990;36:1299-1312.
37. Hartzog DG, Sircar S. Sensitivity of PSA process performance to input variables. *Adsorption.* 1995;1:133-151.
38. Lu ZP, Loureiro JM, LeVan MD, Rodrigues AE. Pressure swing adsorption processes: intraparticle diffusion/convection models. *Indus Eng Chem Res.* 1993;32:2740-2751.

Manuscript received July 4, 2005, and revision received Jun. 12, 2006.